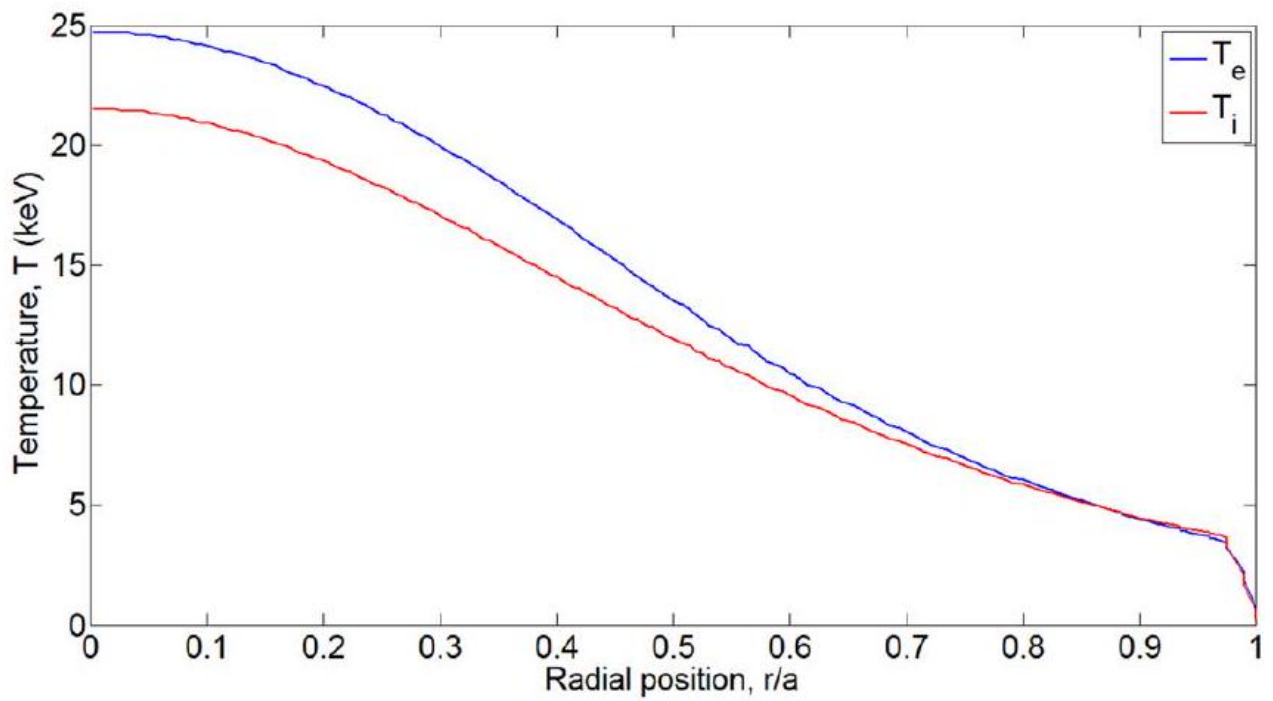
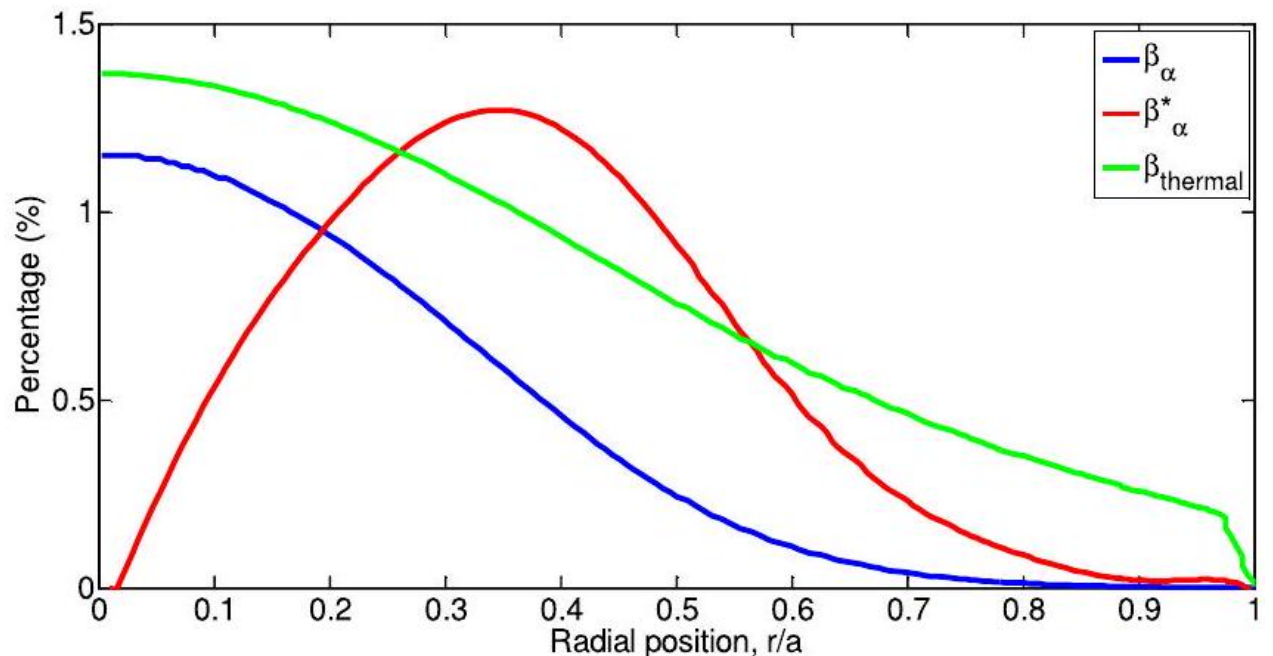


**Figure 1:** Density profiles of electrons (blue), DT mixture (green), and He (red) versus normalized radius for the ITER 15 MA baseline scenario.



**Figure 2:** Profiles of electron temperature (blue) and DT ion temperature (red) versus normalized radius.



**Figure 3:** Profiles of  $\beta_\alpha$  (%), normalised gradient of alpha-particle pressure  $\beta_\alpha^* = -ad\beta_\alpha/dr$  and thermal plasma  $\beta$  in the 15MA ITER baseline scenario considered versus normalized radius.

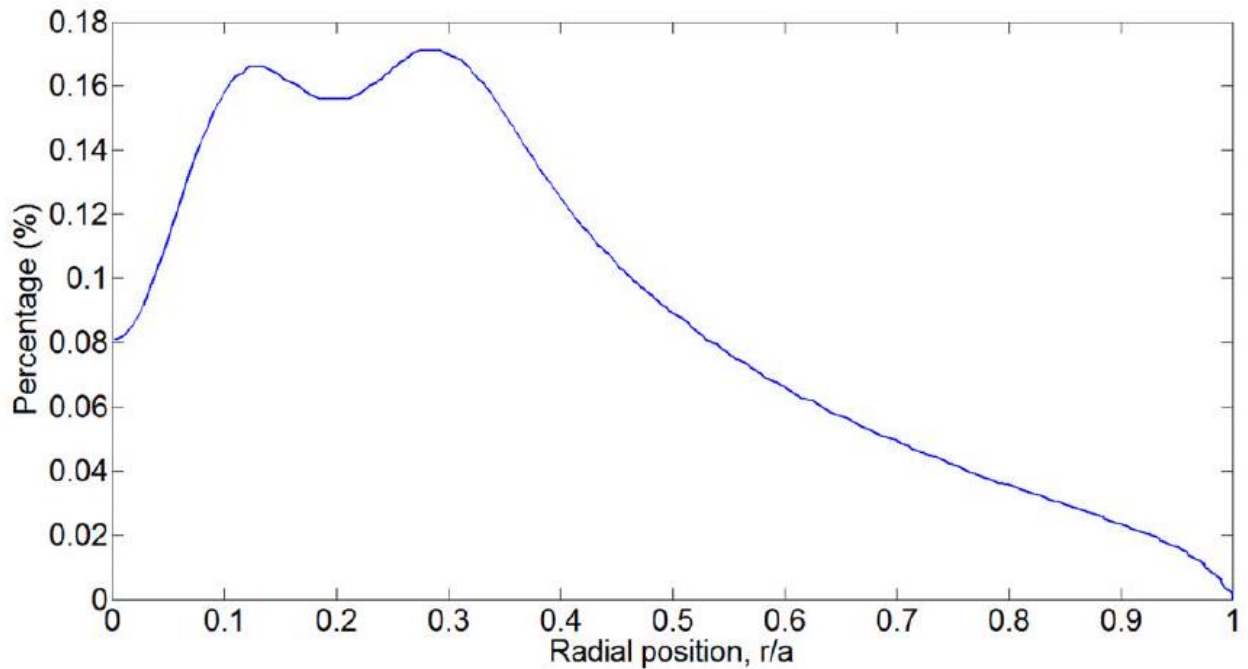


**Figure 4:** Profile of  $\beta_{beam}$  (%) in the 15MA ITER baseline scenario considered versus normalized radius. beam ion profiles for the  $Q = 10$  operational point. The energetic alpha-particle and beam populations are computed using a Fokker-Planck approach.

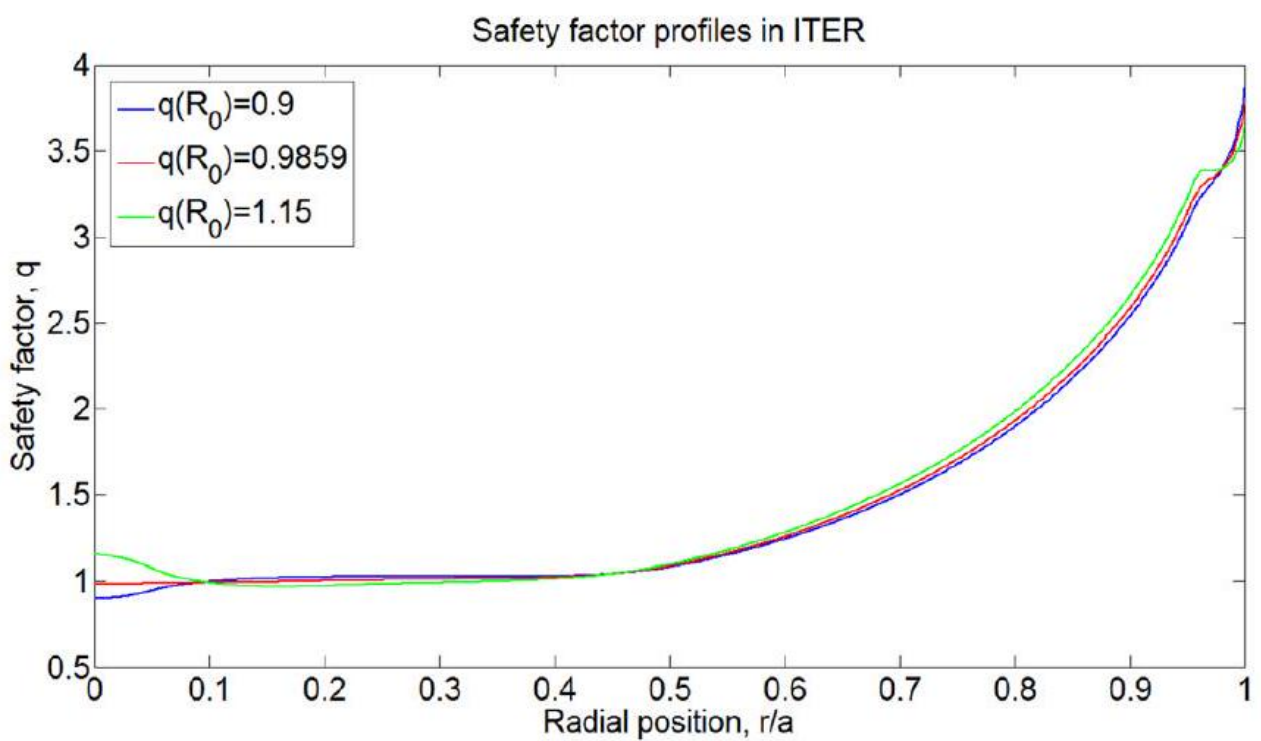


**Figure 5:**  $q(r)$ -profiles in the 15 MA scenario considered versus normalized radius.

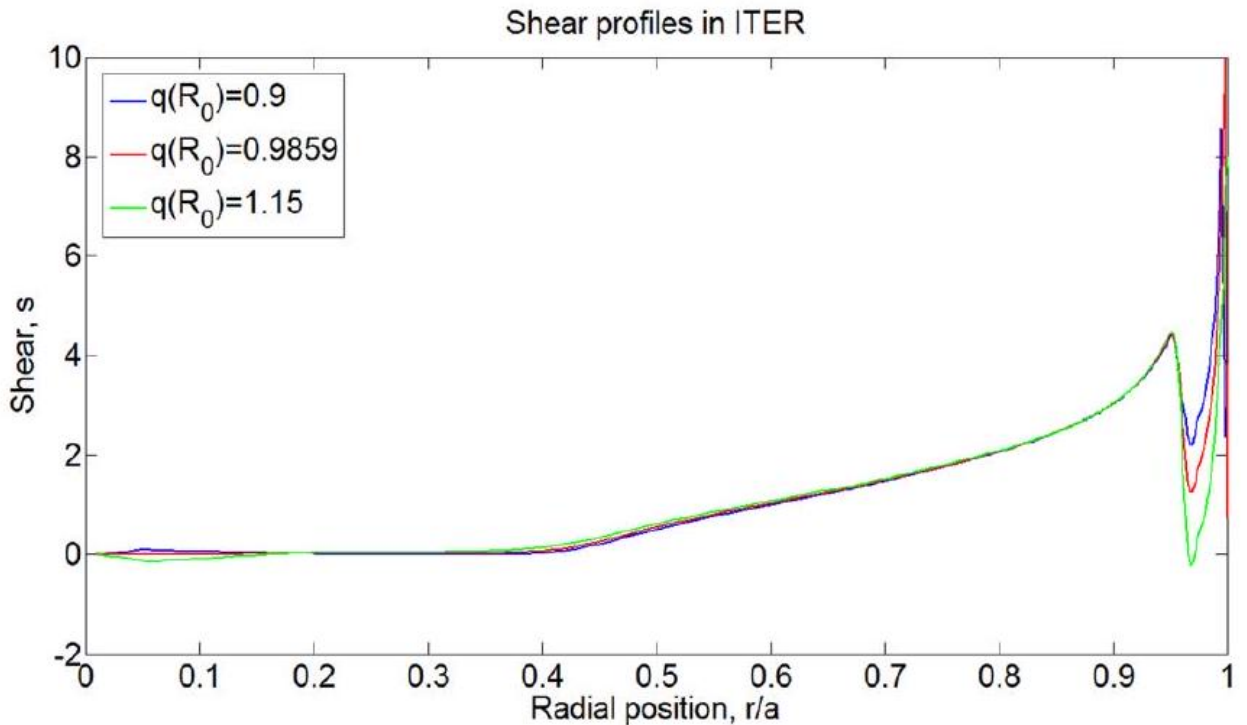


**Figure 6:** Profiles of the magnetic shear in the 15 MA scenario considered versus normalized radius.

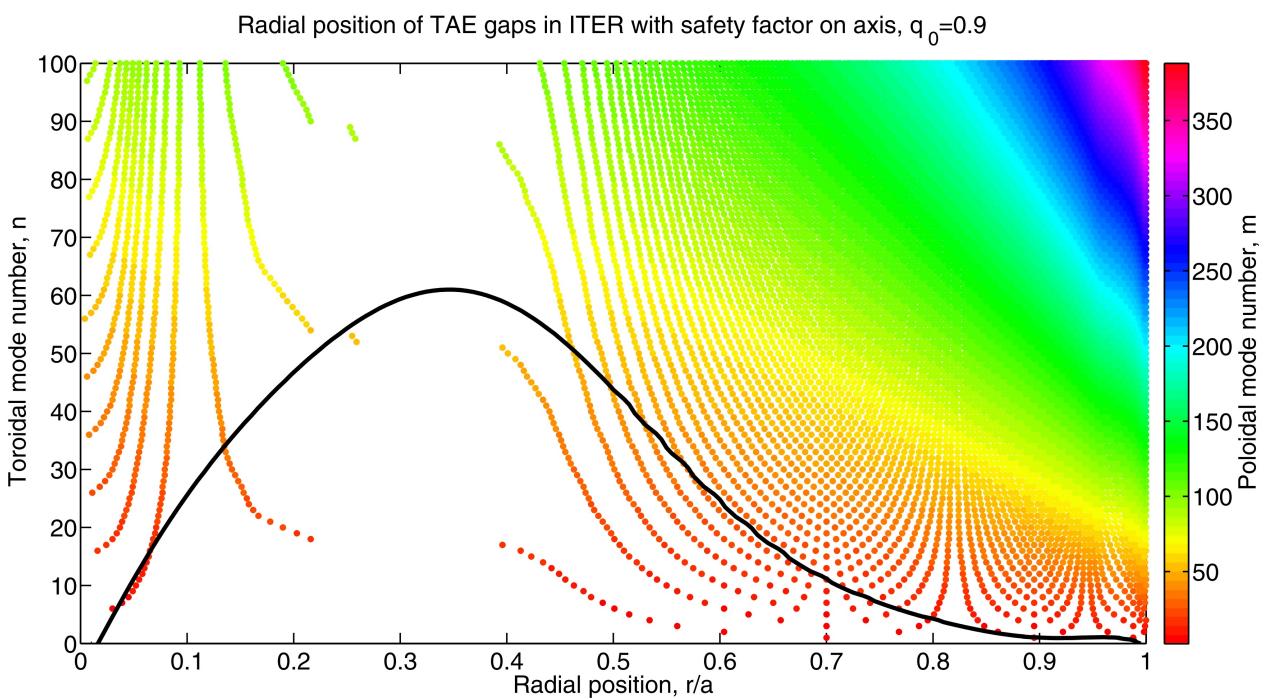


**Figure 7:** Radial localisation of TAE gaps in ITER with  $q_0 = 0.9$ . The solid line shows the normalised radial gradient of alpha-particle pressure.

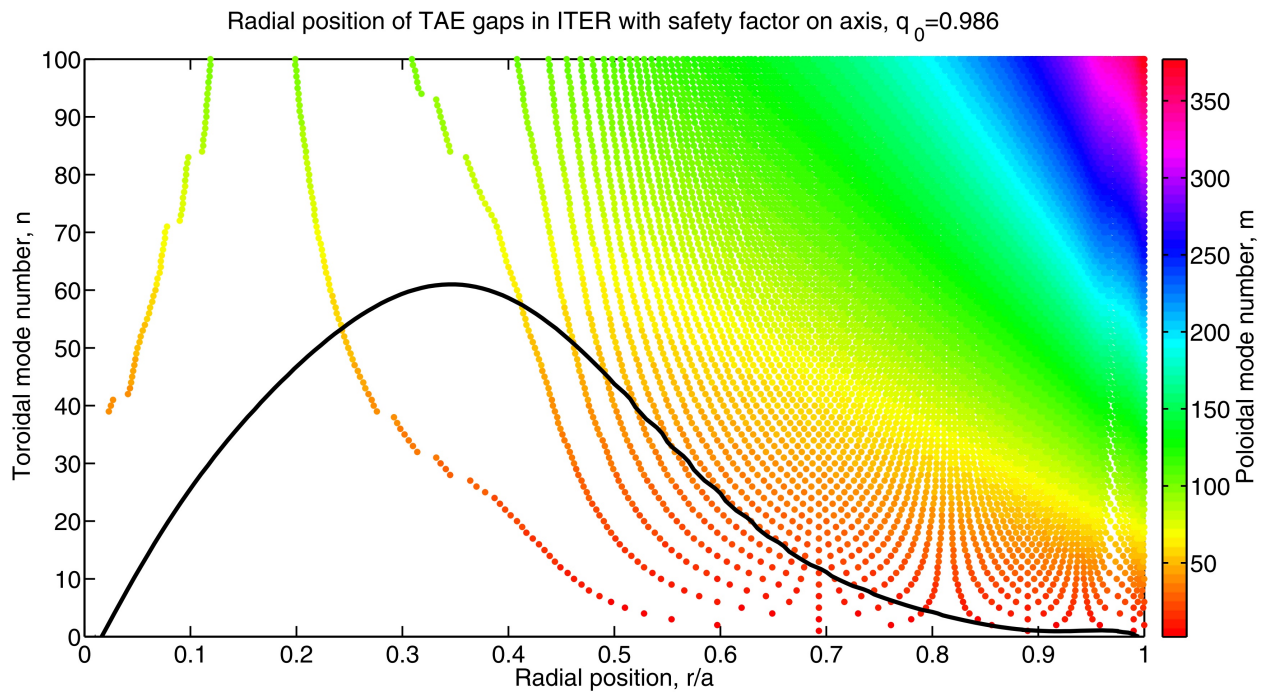


**Figure 8:** Radial localisation of TAE gaps in ITER with  $q_0 = 0.986$ .

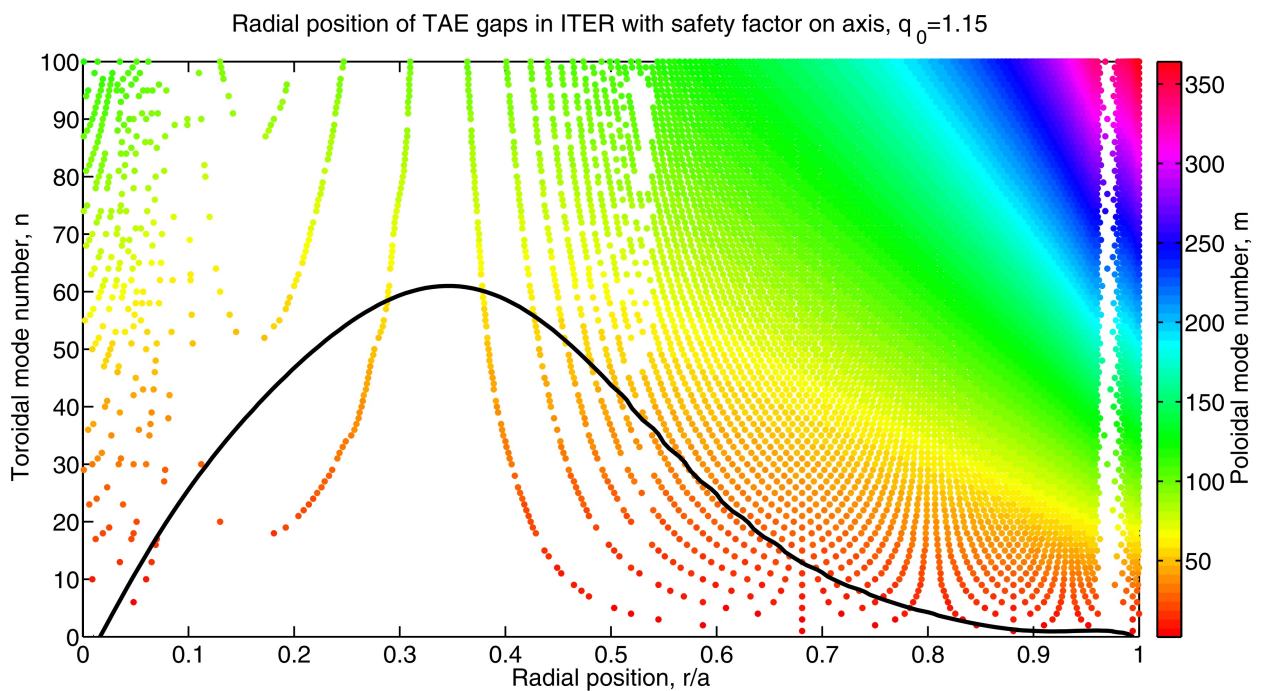


**Figure 9:** Radial localisation of TAE gaps in ITER with  $q_0 = 1.15$ .

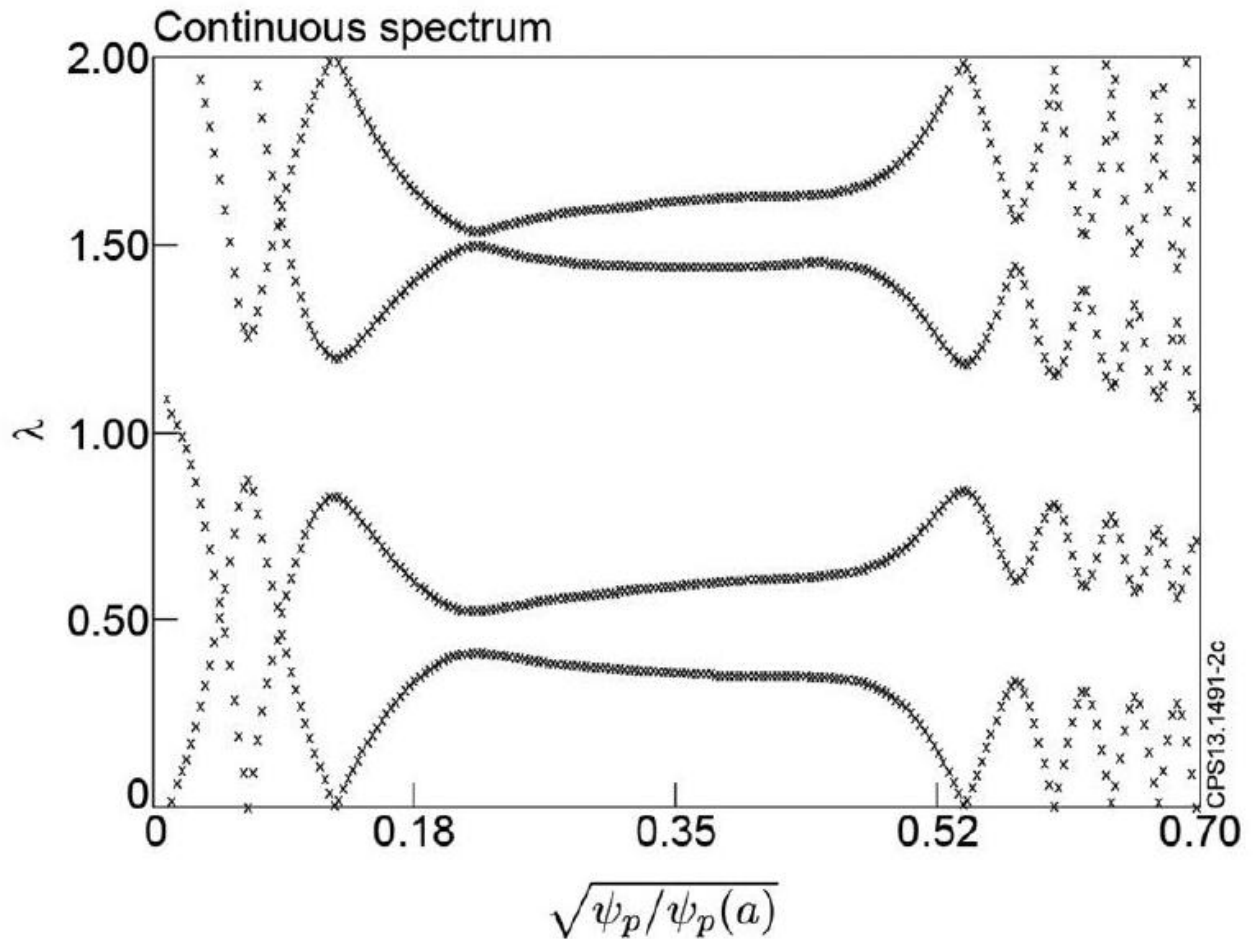


**Figure 10:** Radial structure of the  $n = 20$  Alfvén continuum in a 15MA ITER baseline case with  $q(0) = 0.9$ . Here,  $\lambda = \omega R_0/V_A(0)$  and  $\sqrt{\psi_p/\psi_p(\text{edge})} \approx r/a$ .

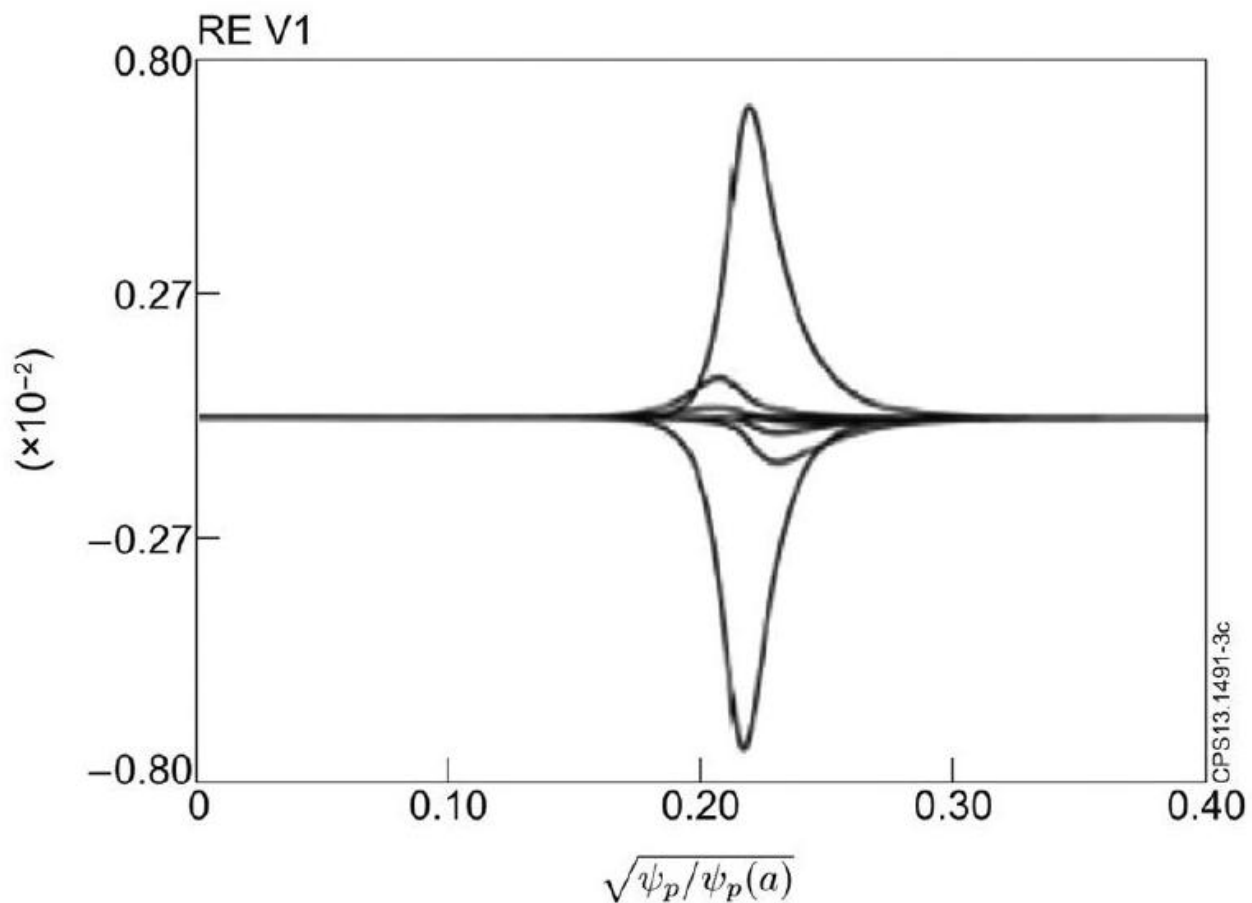


**Figure 11:** Upper core-localised TAE with  $n = 20$  and  $\lambda = 0.525$  in the 15MA ITER baseline case with  $q(0) = 0.9$ . Here,  $V_1 = s \cdot V_r$ ,  $V_r$  is the radial velocity component and  $\sqrt{\psi_p/\psi_p(\text{edge})} \approx r/a$ .

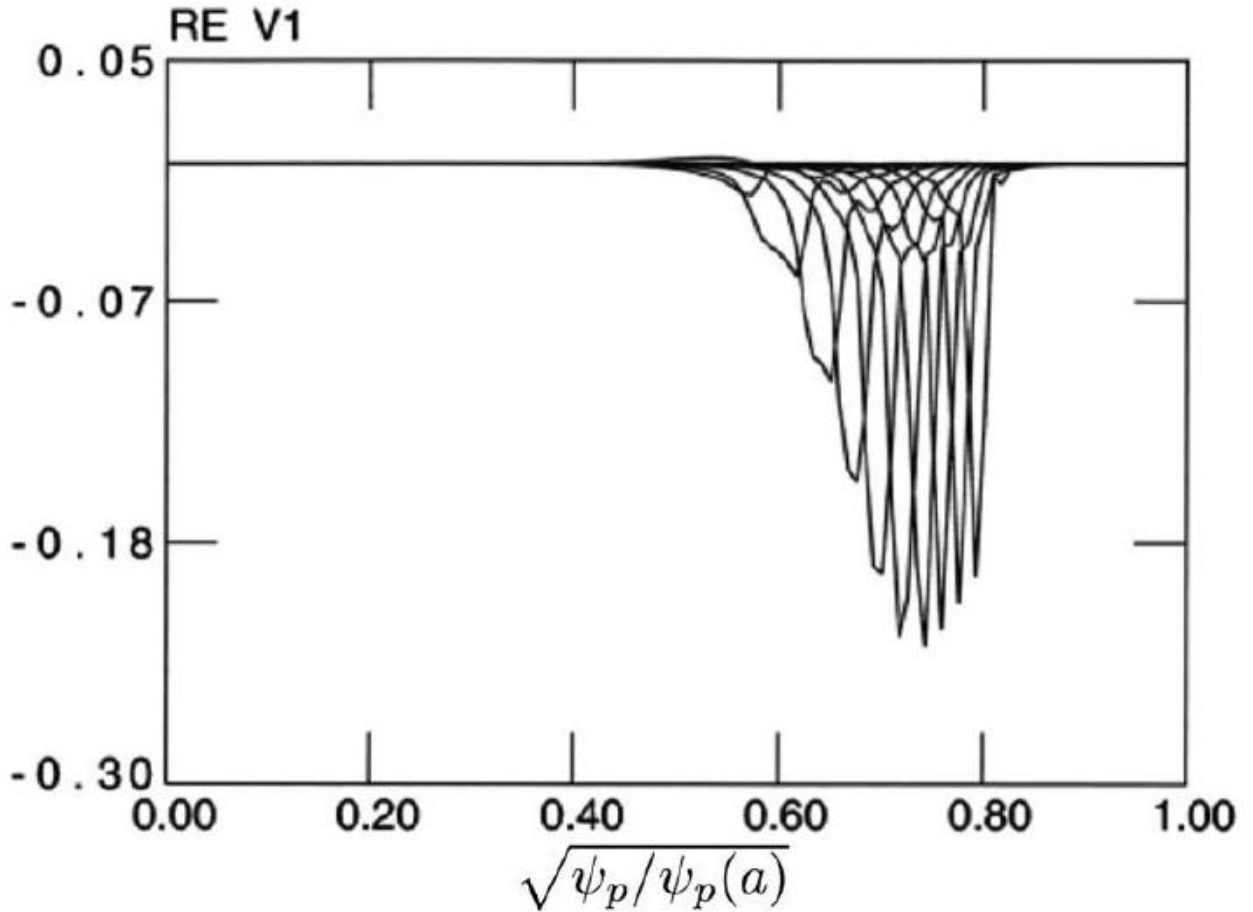


**Figure 12:** Global TAE with  $n = 20$  and  $\lambda = 0.447$  in the 15MA ITER baseline case with  $q(0) = 0.9$ .

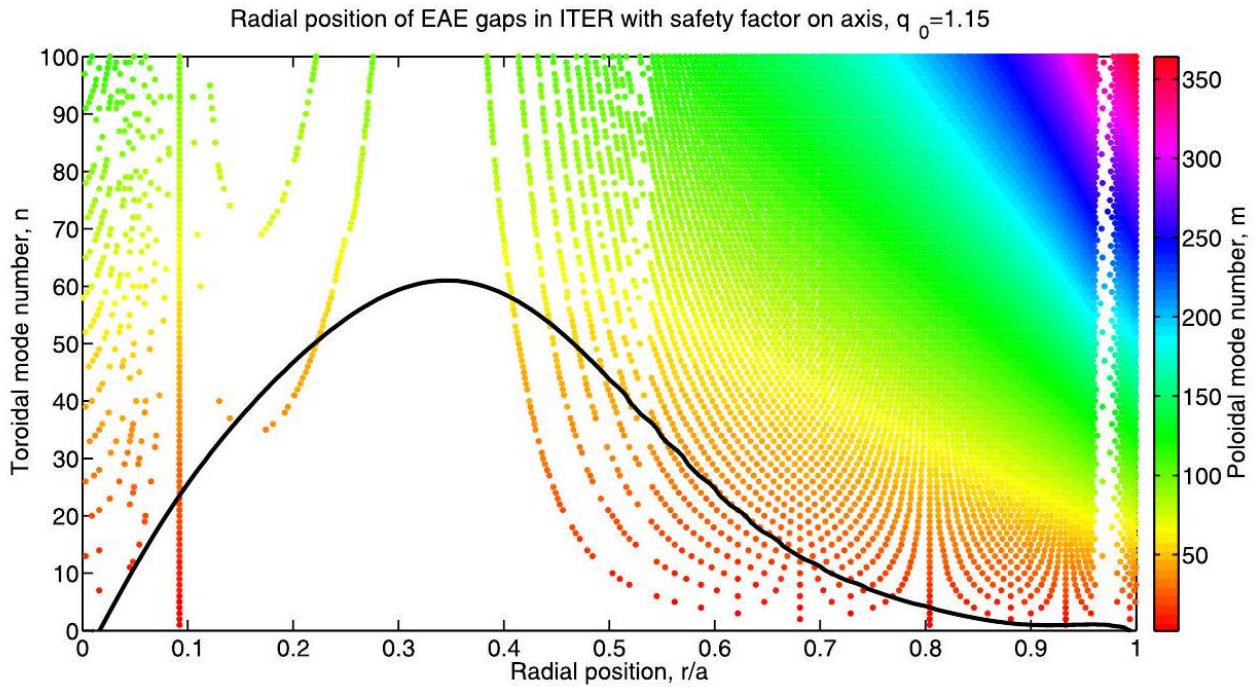


**Figure 13:** Radial localisation of EAE gaps in the 15 MA ITER baseline case with  $q(0) = 1.15$ .

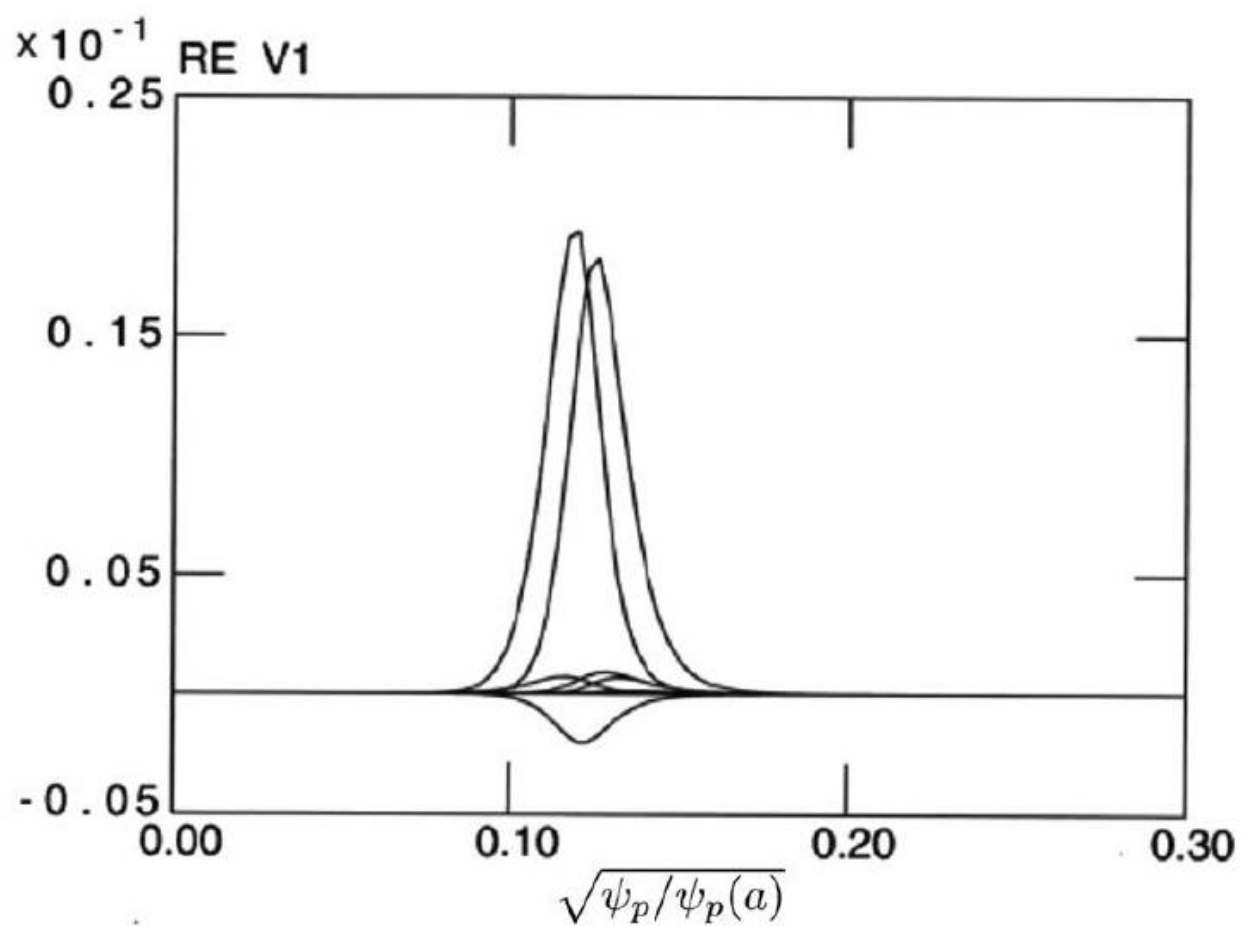


**Figure 14:** Core-localised EAE with  $n = 20$  and  $\lambda = 1.15$  in 15MA ITER baseline case with  $q(0) = 0.9$ .

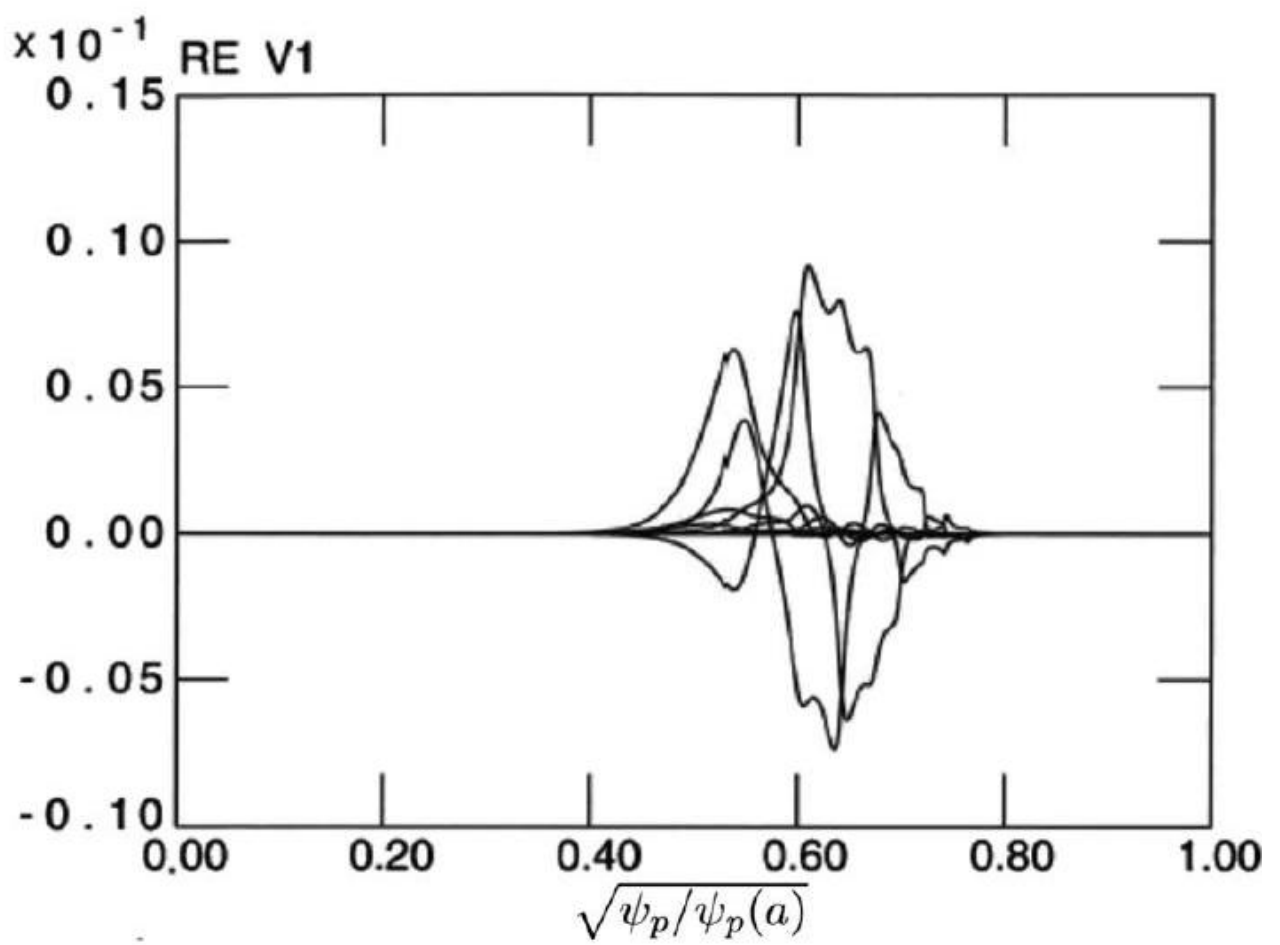


**Figure 15:** Global EAE with  $n = 20$  and  $\lambda = 1.036$  in 15MA ITER baseline case with  $q(0) = 0.9$ .

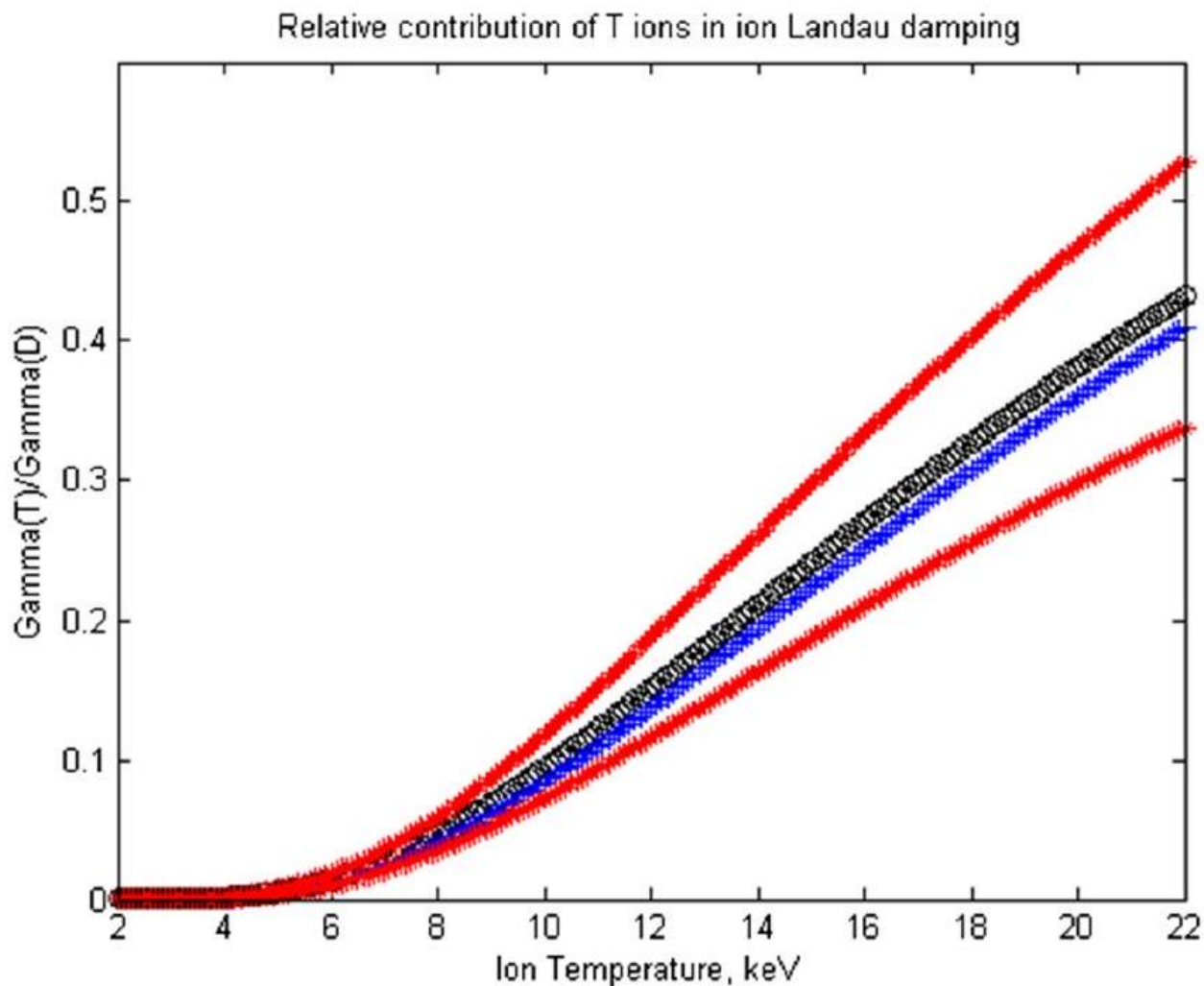


**Figure 16:** Ratio of T ion Landau damping to D ion Landau damping as a function of ion temperature. The black line corresponds to  $\mu = \delta = 0$ , the blue line corresponds to  $\mu = 0.2, \delta = 0$ , and the upper and lower red lines correspond to  $\mu = 0$  and  $\delta = -0.2$  and  $\delta = +0.2$ , respectively. Coupling Integral ( $D$ )

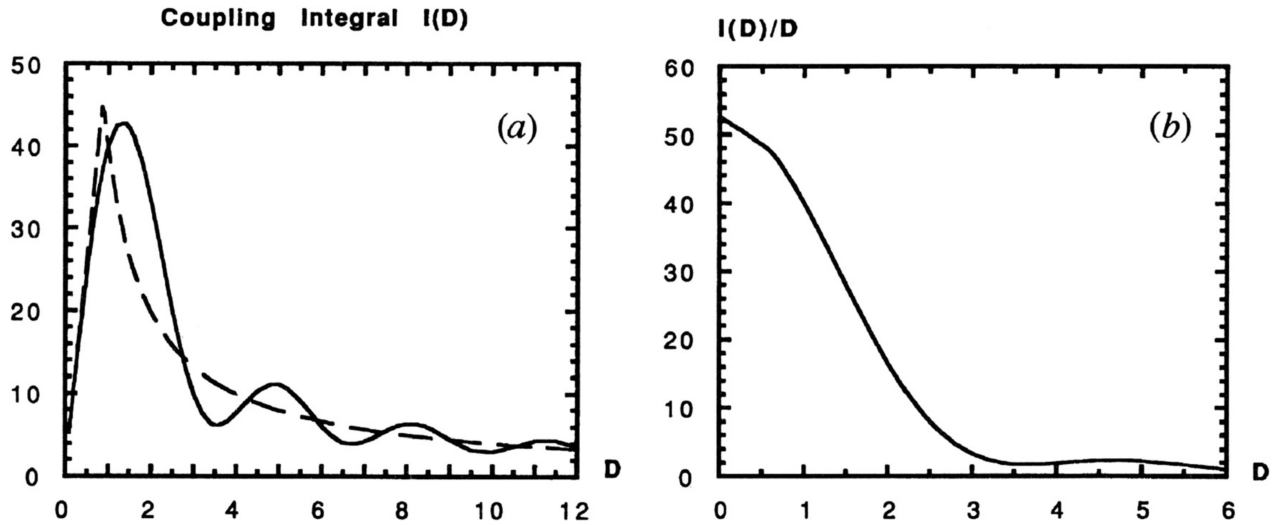


**Figure 17:** Coupling integral  $I(D)$  for passing alpha-particle principal resonances: (a) asymptotic expression (broken curve) and numerical result (full curve); (b) function  $I(D)/D$  used in Eq. (22). Reprinted with permission from B. N. Breizman and S. E. Sharapov, "Energetic particle drive for toroidicity-induced Alfvén eigenmodes and kinetic toroidicity-induced Alfvén eigenmodes in a low-shear tokamak," *Plasma Phys. Controlled Fusion* 37(10), 1057 (1995). Copyright 1995 IOP Publishing. Reproduced by permission of IOP Publishing. All rights reserved.

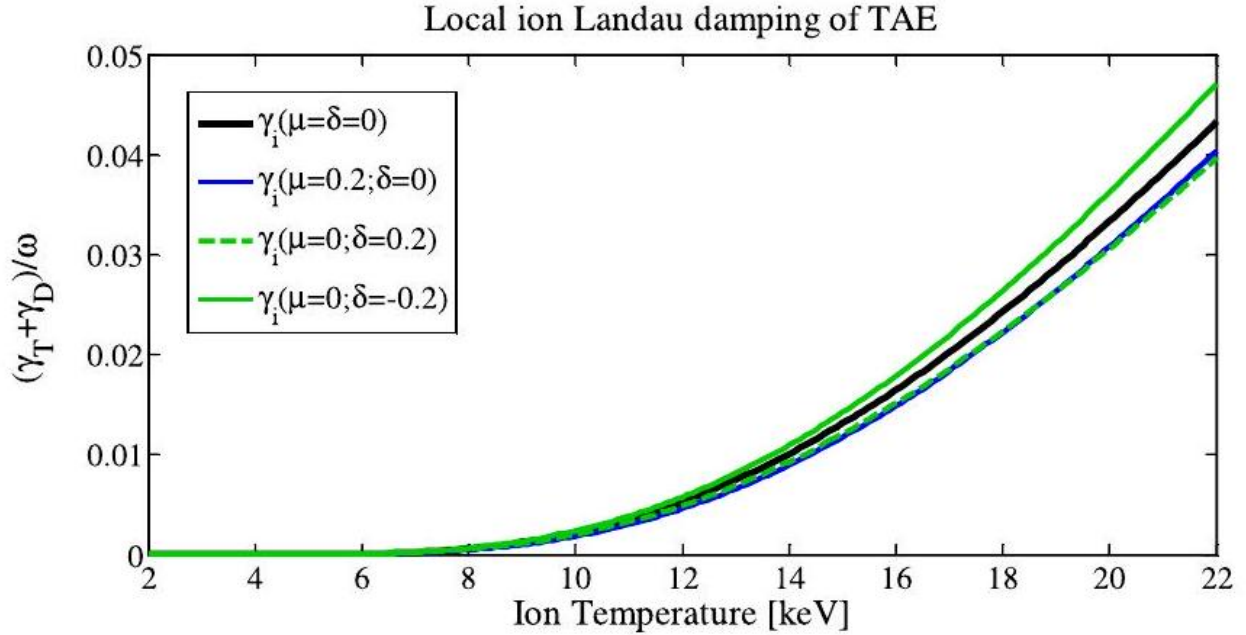


**Figure 18:** Local Landau damping of TAE,  $|\gamma_D + \gamma_T|/\omega$ , as a function of ion temperature. Maxwellian distributions of thermal D and T ions are assumed, and the resonances  $V_{||i} = V_A/3$  between TAE and the ions are considered. The black line corresponds to  $\mu = \delta = 0$ , the blue line corresponds to  $\mu = 0.2, \delta = 0$ , and the upper and lower green lines correspond to  $\mu = 0$  and  $\delta = -0.2$  and  $\delta = +0.2$ , respectively.

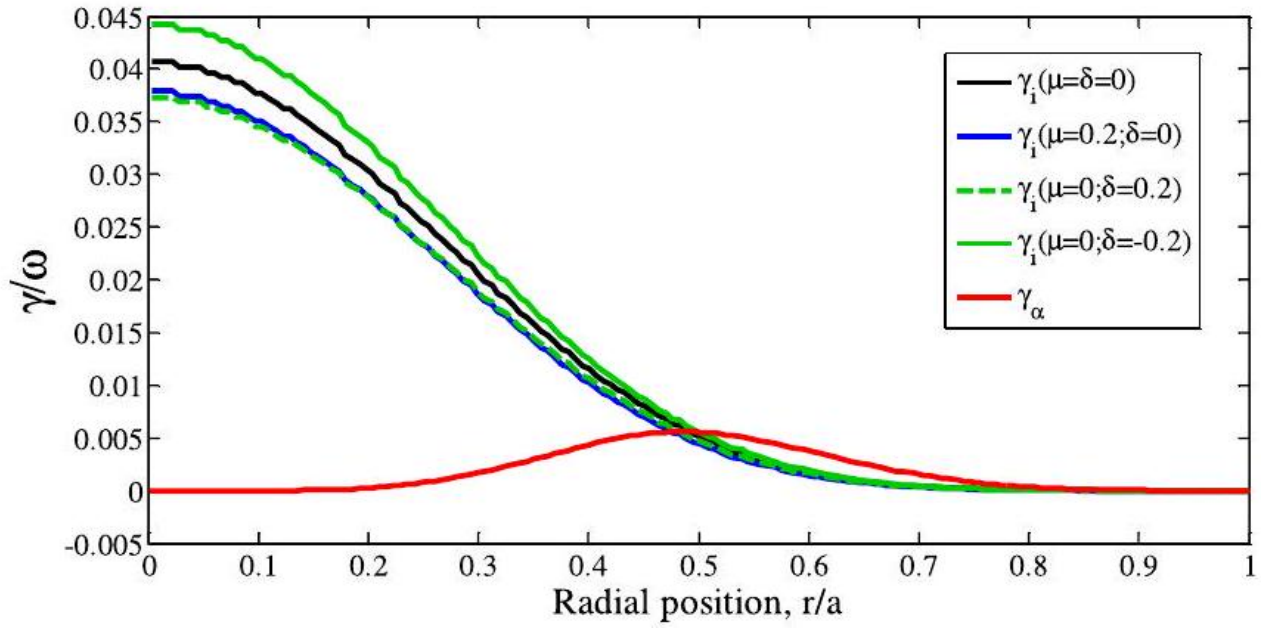


**Figure 19:** Local Landau damping of TAE due to D and T ions and alphaparticle drive versus normalized radius. The alpha-particle drive is shown in red, while the black line corresponds to the ion Landau damping at  $\mu = \delta = 0$ , the blue line corresponds to  $\mu = 0.2, \delta = 0$ , and the two green lines correspond to  $\mu = 0, \delta = \pm 0.2$ .

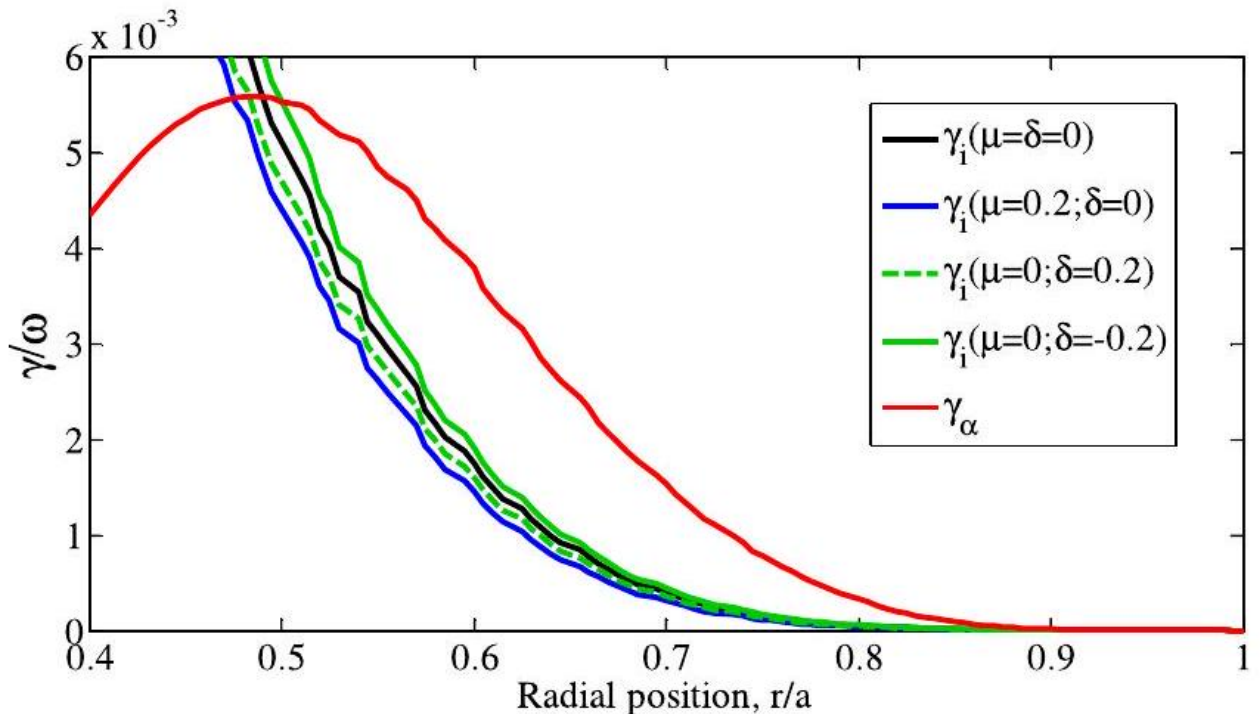


**Figure 20:** Zoom of Figure 19. Local Landau damping of TAE due to D and T ions (black line:  $\mu = \delta = 0$ ; blue line:  $\mu = 0.2, \delta = 0$ ; and green lines:  $\mu = 0, \delta = \pm 0.2$ ) and alpha-particle drive (red line) versus normalized radius for  $0.4 \leq r/a \leq 1.0$ .

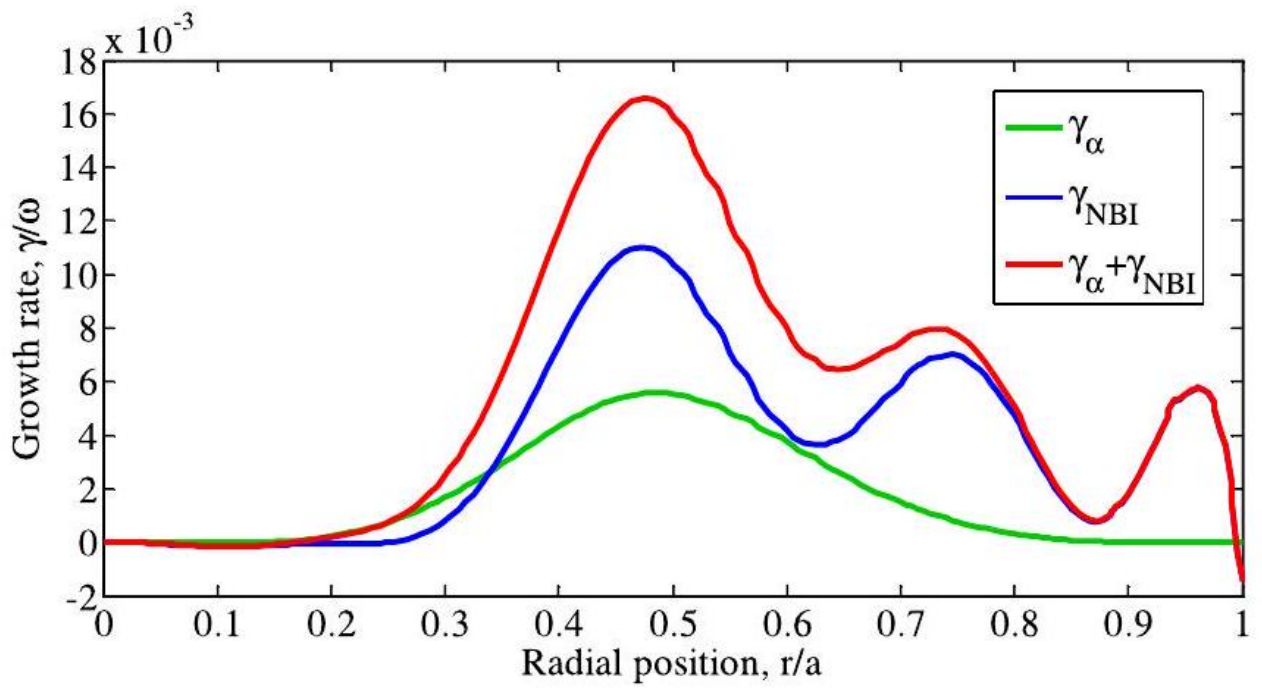


**Figure 21:** Alpha-particle drive (green) and NBI-drive (blue) and sum of the two (red) versus normalized radius.

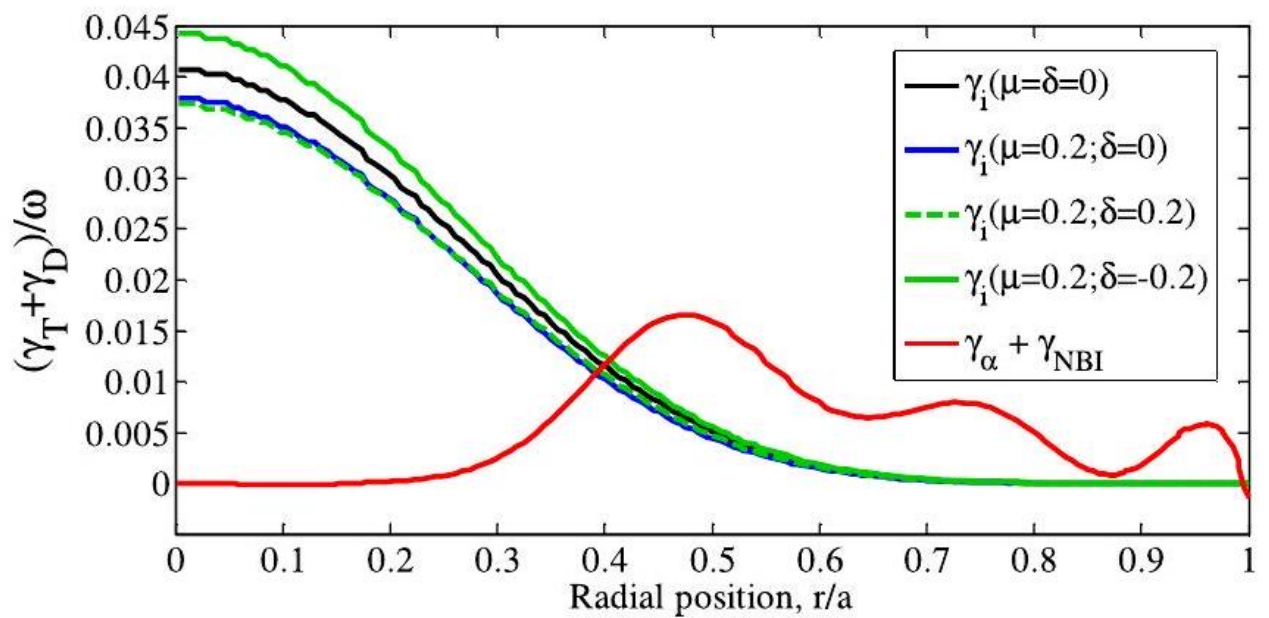


**Figure 22:** The sum of alpha-particle and beam drives (red) versus ion Landau damping, as shown in Figure 19, versus normalized radius.

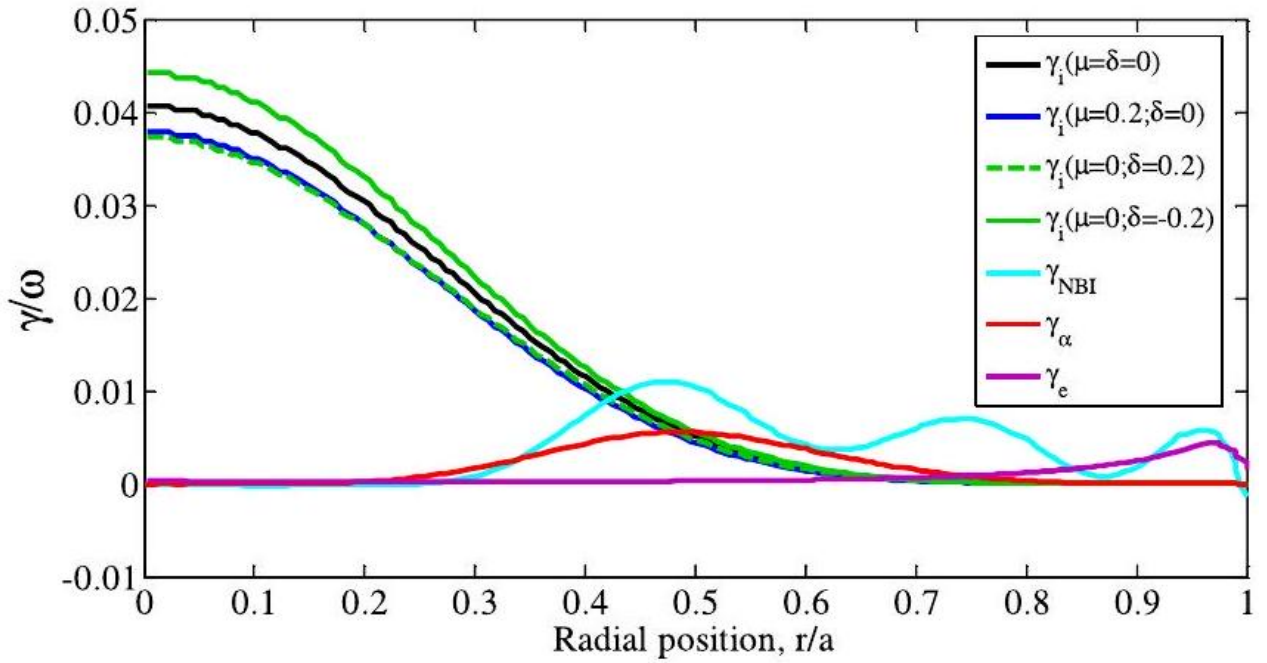


**Figure 23:** Trapped electron collisional damping (purple). Local Landau damping of TAE due to D and T ions as shown in Figure 19, alpha-particle drive (red) and beam drive (cyan). radiative damping significantly unless the mode frequency is close to the top of the TAE gap. [18] In general, a kinetic analysis is required for assessing the role of the radiative damping, but analytical expressions may be used in the limiting cases of small and large magnetic shear. In particular, for TAE with frequencies at the bottom of the gap, the following expressions may be used: [24]

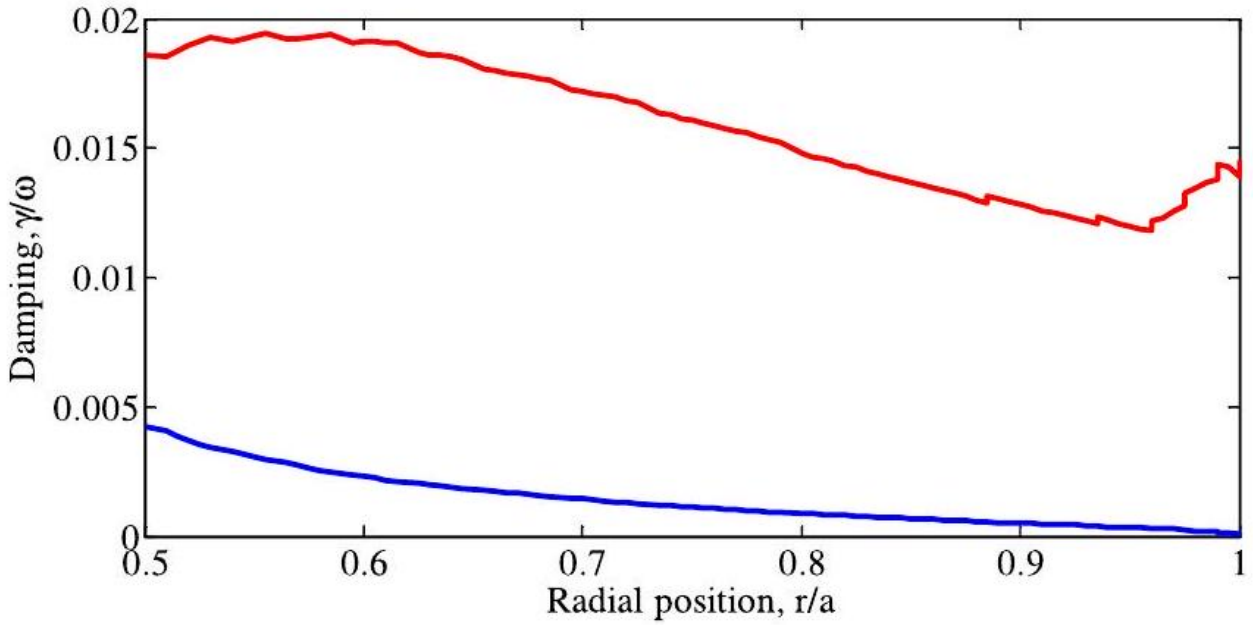


**Figure 24:** Analytic expressions for the radiative (blue) and continuum (red) damping effects corresponding to the high-shear region. A closed TAE frequency gap is assumed when calculating the continuum damping. (shown in Figure 10), Eq. (30) would indeed provide a reasonably high damping rate in the external region of interest. Figure 24 shows that in this case, the damping could be in the range of 1.2% – 1.9%, i.e., in excess of the net drive shown in Figure 23.

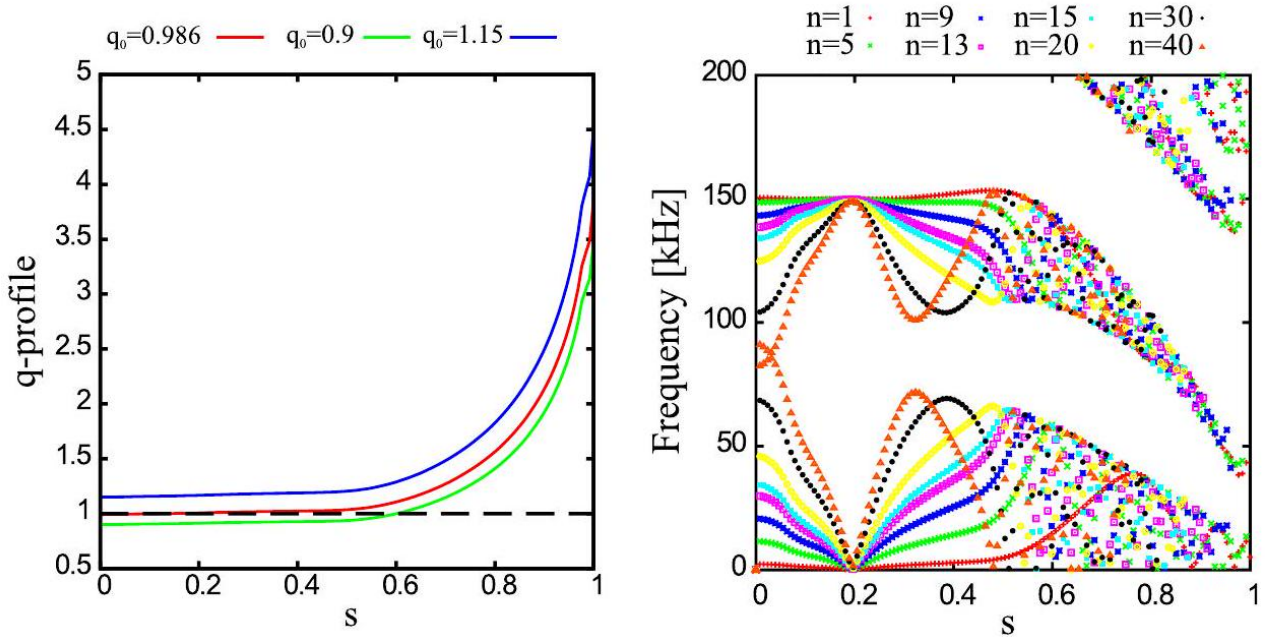


**Figure 25:** Left: The different *q*-profiles used in the simulations versus the normalized poloidal radius *s*; right: Ideal SAW continuum for  $q_0 = 0.986$  versus the normalized poloidal radius *s*.

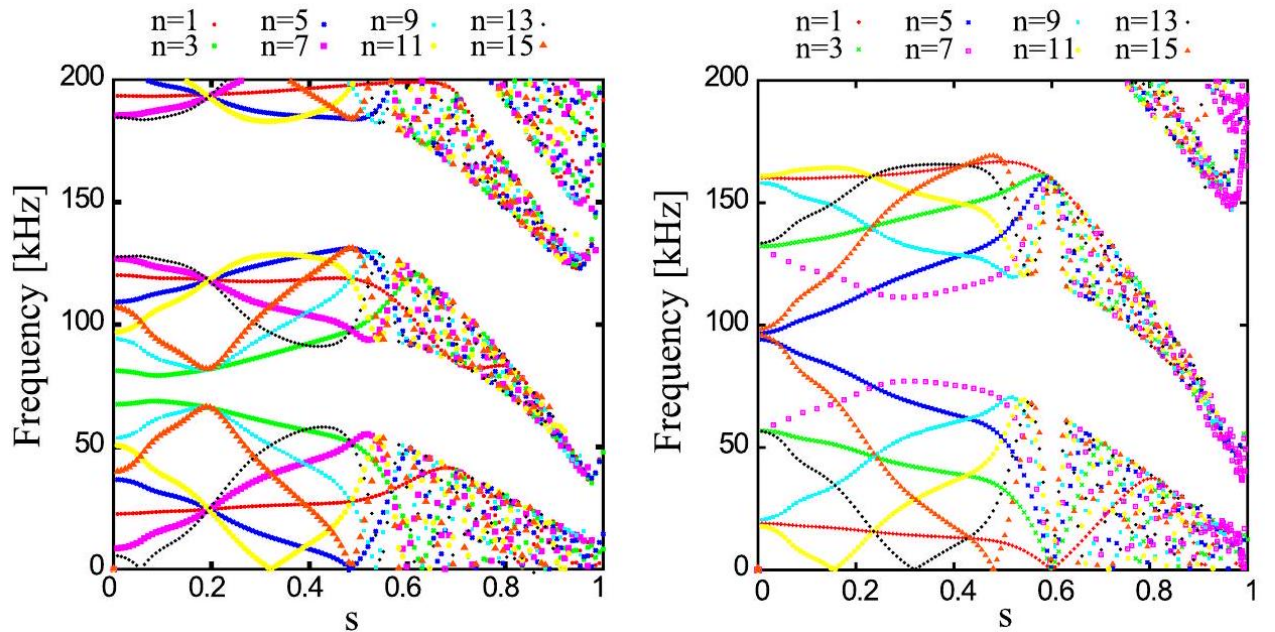


**Figure 26:** Left: Ideal SAW continuum for  $q_0 = 1.15$  versus the normalized poloidal radius *s*; right: Ideal SAW continuum for  $q_0 = 0.9$  versus the normalized poloidal radius *s*.

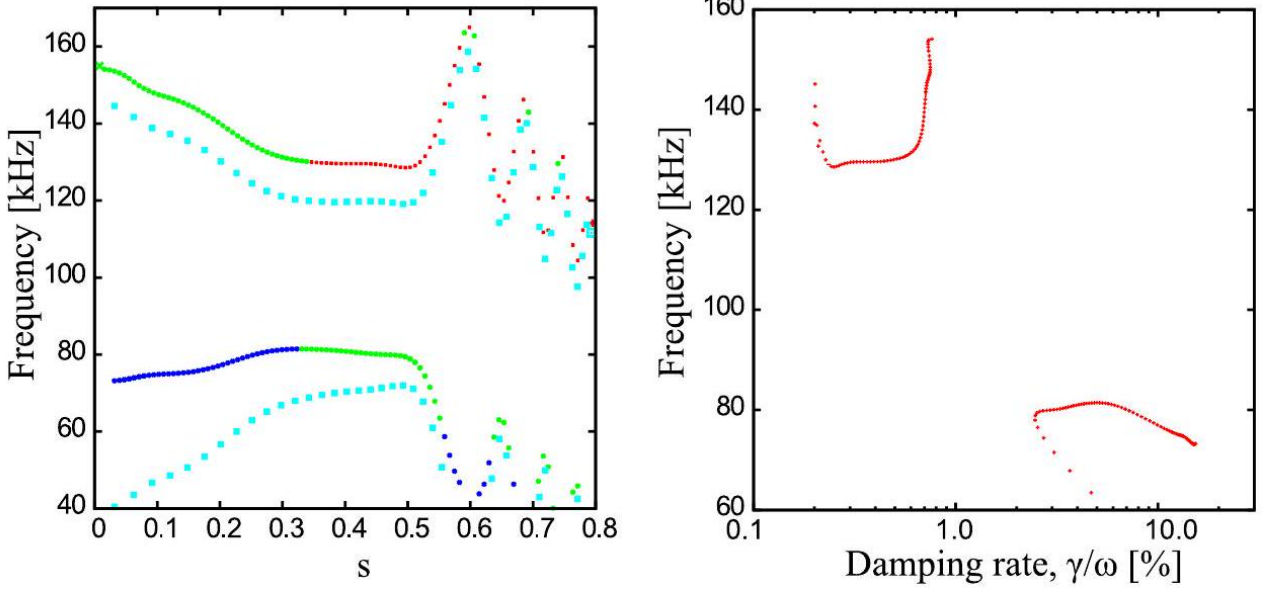


**Figure 27:** Left: Kinetic continuum for  $n = 8$  and  $q_0 = 0.9$  versus the normalized poloidal radius  $s$ . In light blue, the reduced MHD calculation, in red the part of the continuum that has a damping less than  $\gamma/\omega < 0.5\%$ , in green  $0.5\% < \gamma/\omega < 5\%$  and in dark blue  $\gamma/\omega > 5\%$ ; right: The upper and lower TAE continuum branches as on the left as a function of the local damping. For a local estimate, the damping at the accumulation points ( $\sim 125$ kHz for the anti-symmetric branch and  $\sim 85$ kHz for the symmetric branch) can be used. The damping is quite different: 0.3% vs. 5%.

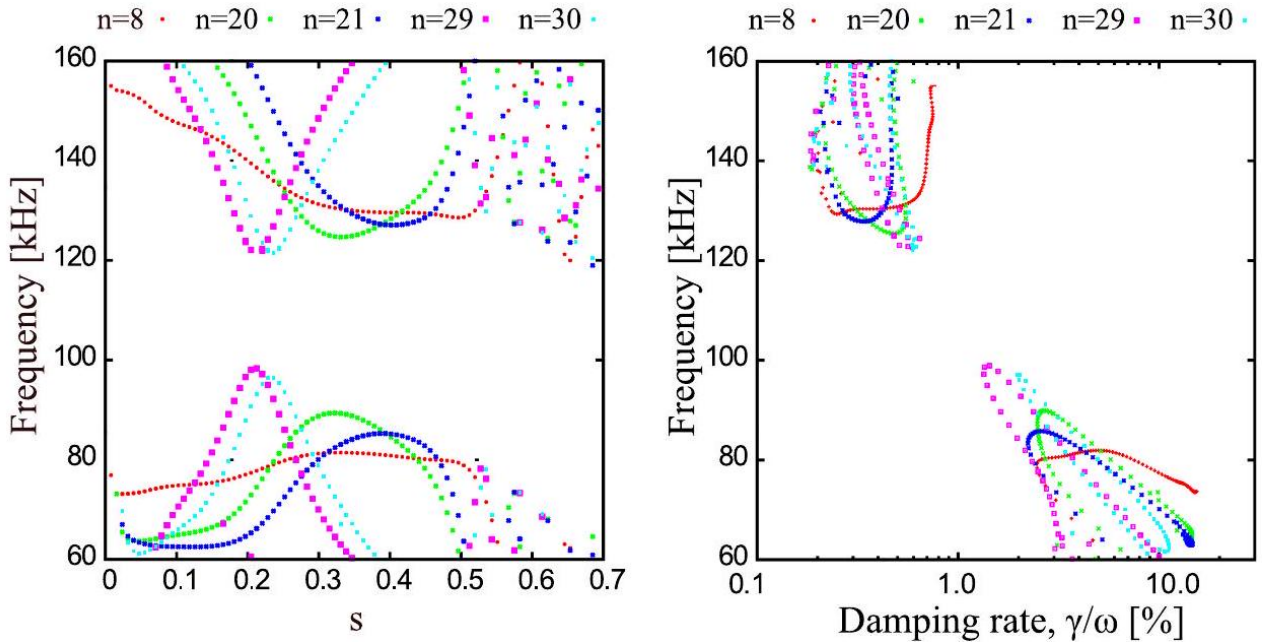


**Figure 28:** Left: Kinetic continuum for  $n = 8, 20, 21, 29, 30$  and  $q_0 = 0.90$ . Right: The upper and lower TAE continuum branches as on the left as a function of the local damping.

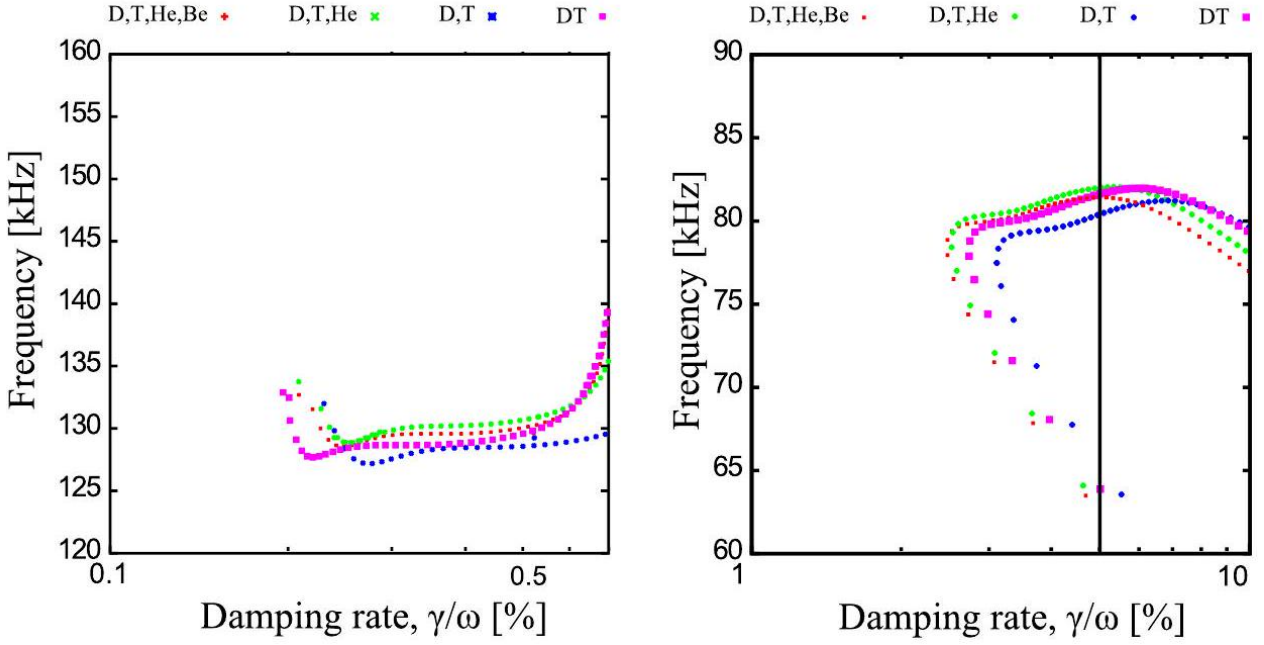


**Figure 29:** Left: Kinetic continuum for the  $n = 8$  anti-symmetric TAE branch for different isotope mixtures. There is a weak dependence of the damping at the accumulation point on different background ion components. The profiles of the He ash and the beryllium are as given in Sec. II. Right: Kinetic continuum for the  $n = 8$  symmetric TAE branch. At low frequencies, considerable differences occur: the damping is overestimated by 2.5% if the diluting effects of the background are neglected (compare extrema of red and blue curves).

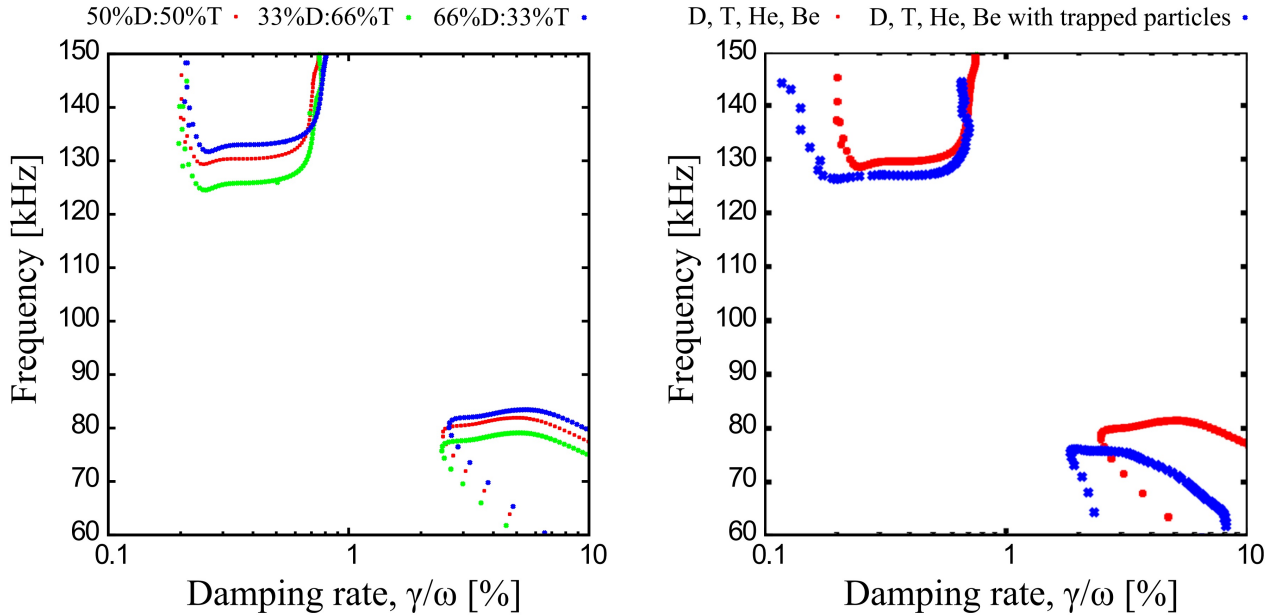


**Figure 30:** Left: Kinetic continuum for the  $n = 8$  symmetric and antisymmetric TAE branch for different D : T mixtures. Although there is a small influence on the real frequency via a change of the mass density, the damping at the continuum accumulation point stays nearly constant. Right: Kinetic continuum for the  $n = 8$  symmetric and anti-symmetric TAE branch including only circulating particles (red) and both circulating and trapped particles (blue). Whereas the higher frequency (odd) branch is not strongly affected, the lower frequency (even) branch shows reduced damping. show very good agreement with the analytic work in Secs. III-VII, both qualitatively and quantitatively.

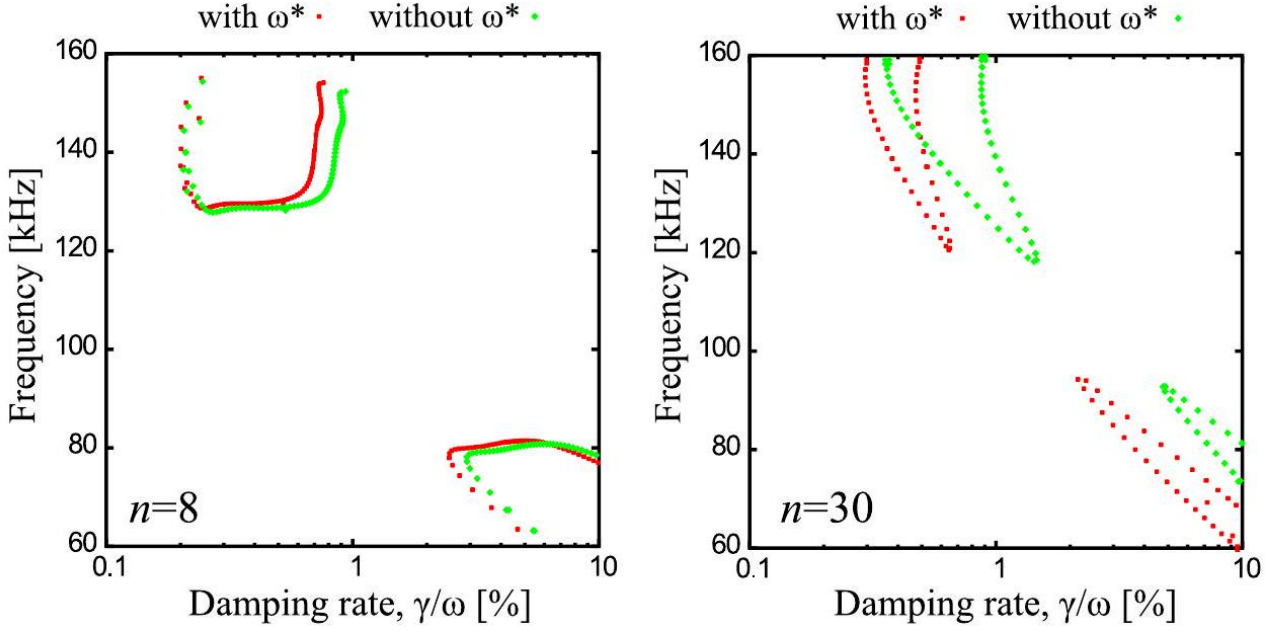


**Figure 31:** Left: kinetic continuum for the  $n = 8, m = 7, 8$  TAE branches with and without  $\omega_p^*$ ; right: kinetic continuum for  $n = 30, m = 29, 30$  with and without  $\omega_p^*$ .

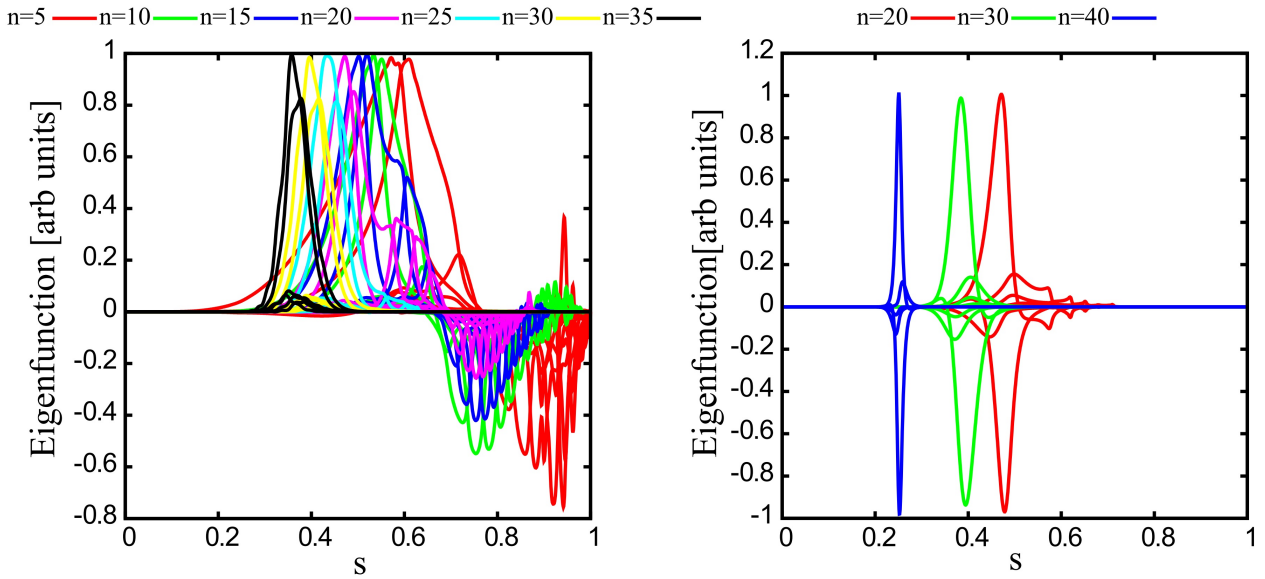


**Figure 32:** Left: Eigenfunctions (electrostatic potential) for symmetric TAEs and  $q_0 = 0.986$ ; right: Eigenfunctions (electrostatic potential) for anti-symmetric TAEs and  $q_0 = 0.9859$ . values. [19,45] The frequency and damping of the symmetric and anti-symmetric  $n = 8$  TAE in Figure 33 are 83.9kHz,  $\gamma/\omega = -0.82\%$  (symmetric) and 123kHz,  $-0.67\%$  (antisymmetric). Adding the alpha particle drive using the  $\beta$  profile given in Figure 3 brings this anti-symmetric mode closer to marginal stability:  $\gamma/\omega = -0.30\%$ . Adding the on-axis NBI drive with the beam  $\beta$ -profile as given in Figure 4 (1MeV birth energy, slowing down model) and an ad hoc model for the pitch angle distribution of the form  $\exp\left\{-(\Lambda - \Lambda_0)^2 / \Delta\Lambda^2\right\}$  with  $\Lambda_0 = 0.2, \Delta\Lambda = 0.4$ , and  $\Lambda = \mu B_0/E$  drives the mode marginally unstable:  $\gamma/\omega = +0.05\%$ . More detailed calculations based on actual scenario modelling output for the velocity space distribution function (expected to have a non-negligible influence) will be the subject of future studies.

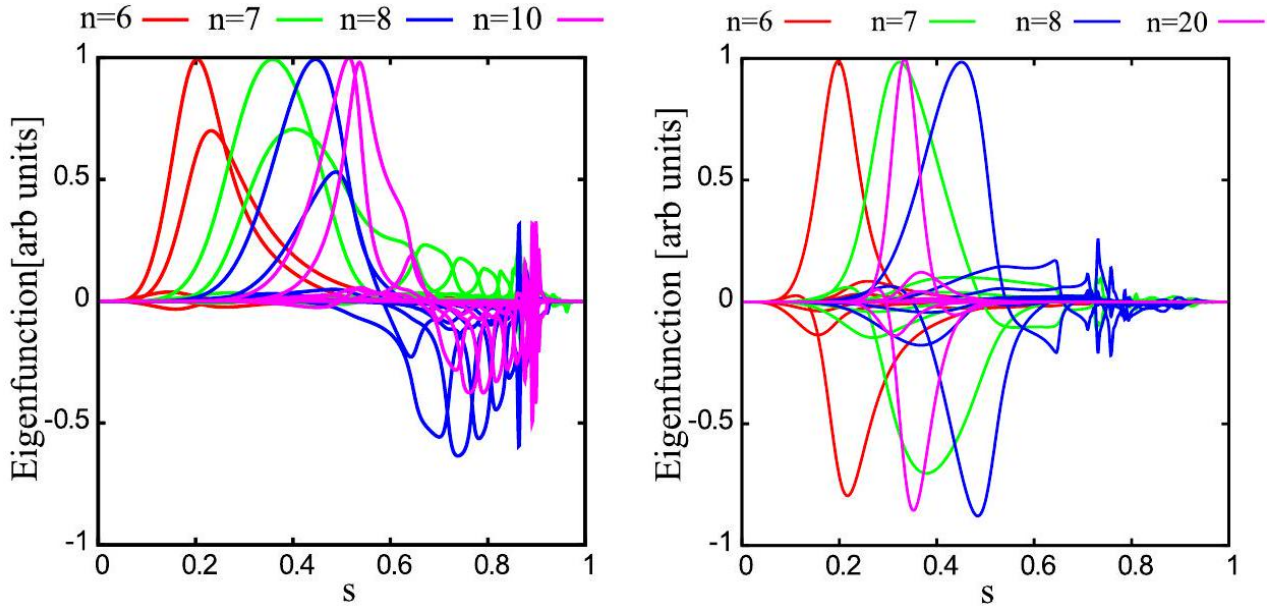


**Figure 33:** Left: Eigenfunctions (electrostatic potential) for low-  $n$  symmetric TAEs and  $q_0 = 0.90$ ; Right: eigenfunctions (electrostatic potential) for low-  $n$  anti-symmetric TAEs and  $q_0 = 0.90$ .

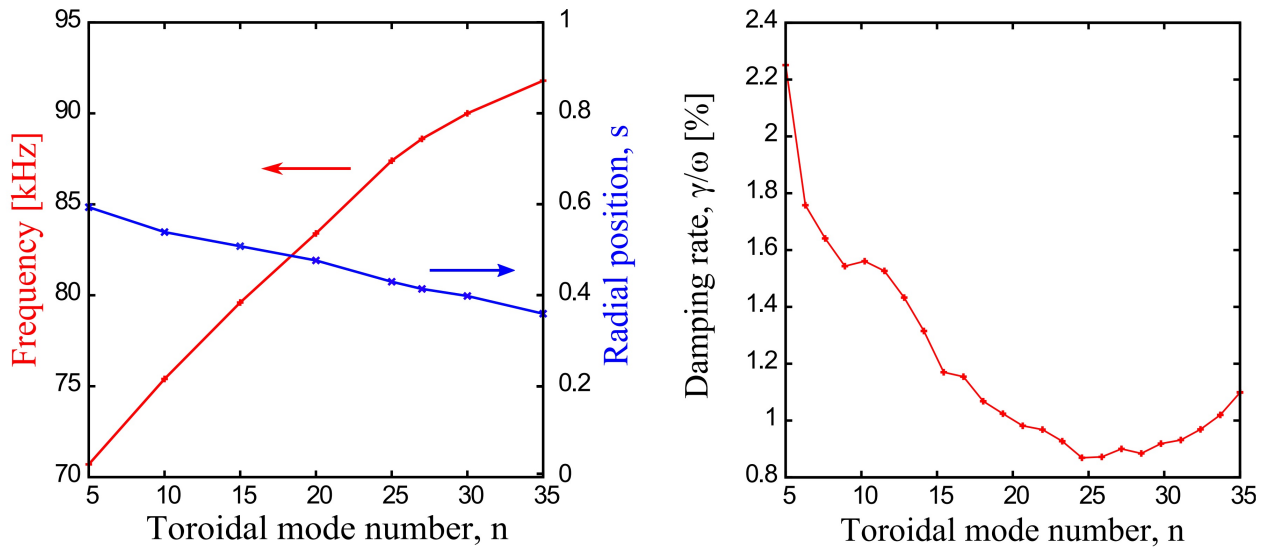


**Figure 34:** Left: TAE frequency and radial position as a function of their toroidal mode number ( $q_0 = 0.985$ ) right: Damping as a function of toroidal mode number. fusion performance would be expected from a quasi-linear estimate. Nevertheless, even a small increase in the energetic particle flux to the first wall is of concern and, therefore, non-linear hybrid simulations will be carried out, on the basis of this stability analysis, in order to understand and quantify possible non-linear effects ("domino effect") that could considerably increase the energetic particle transport in the outer core region and thus also the wall loads.

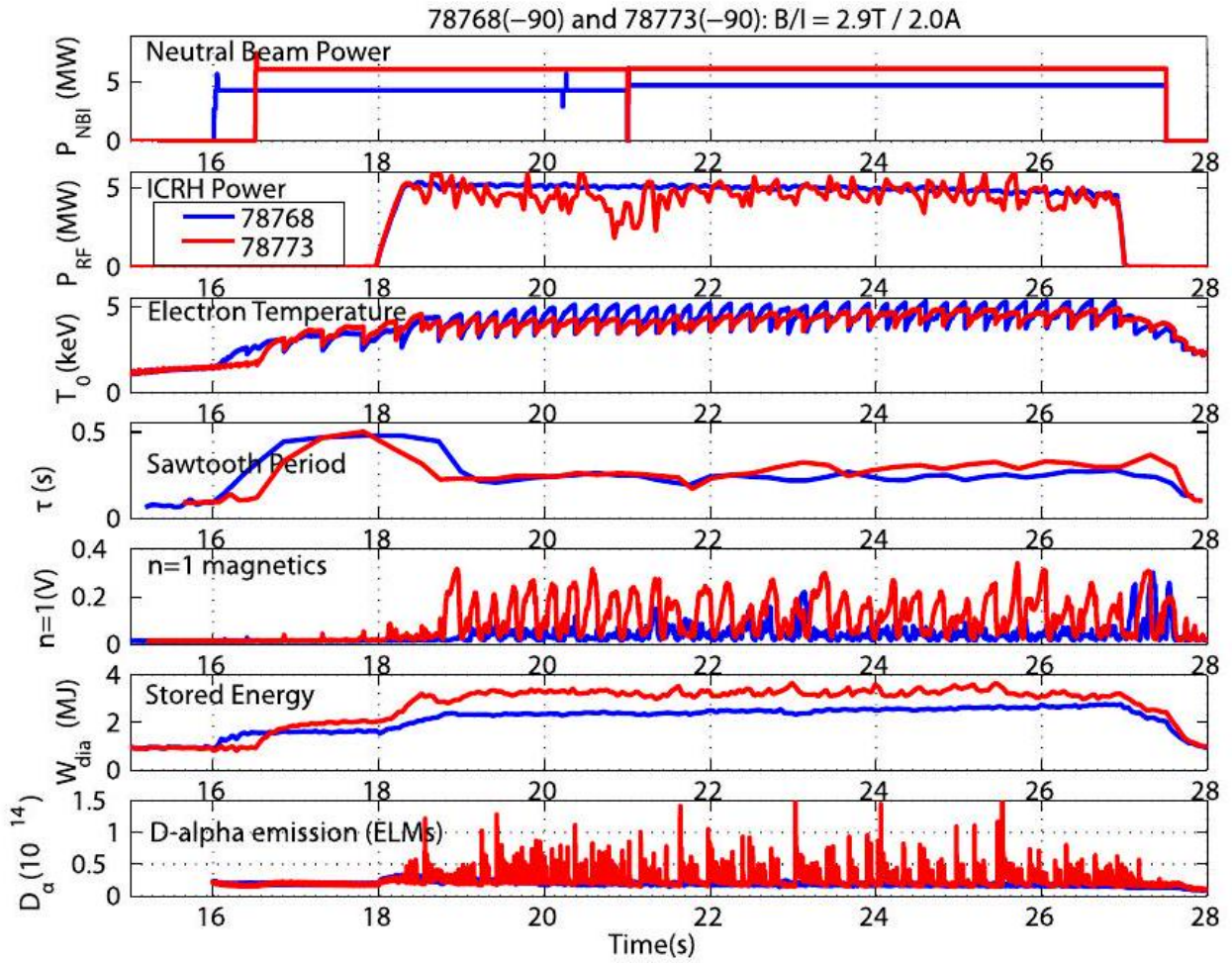


**Figure 35:** JET pulse 78768 (in blue) with 4.8MW of NBI, and JET pulse 78773 (in red) with 6.4 MW of NBI, where both employed low concentration  ${}^3\text{He}$  minority ICRH at around 5MW. In both, the  $-90^\circ$  antenna phasing produces counter current propagating waves, which shorten the sawtooth period, shown by  $\tau$  (s). Also shown is the central electron temperatures in the core, the  $n = 1$  magnetic perturbation amplitude, the stored energy  $W_{dia}$ , and  $D_\alpha$  emission, which indicates that JET pulse 78773 achieves robust sawtooth control even in high confinement mode. Adapted by permission from Macmillan Publishers Ltd: J. P. Graves, I. T. Chapman, S. Coda, M. Lennholm, M. Albergante and M. Jucker, "Control of magnetohydrodynamic stability by phase space engineering of energetic ions in tokamak plasmas," Nature Communications, vol. 3, p. 624, 2012, copyright 2012 (Ref. 75).

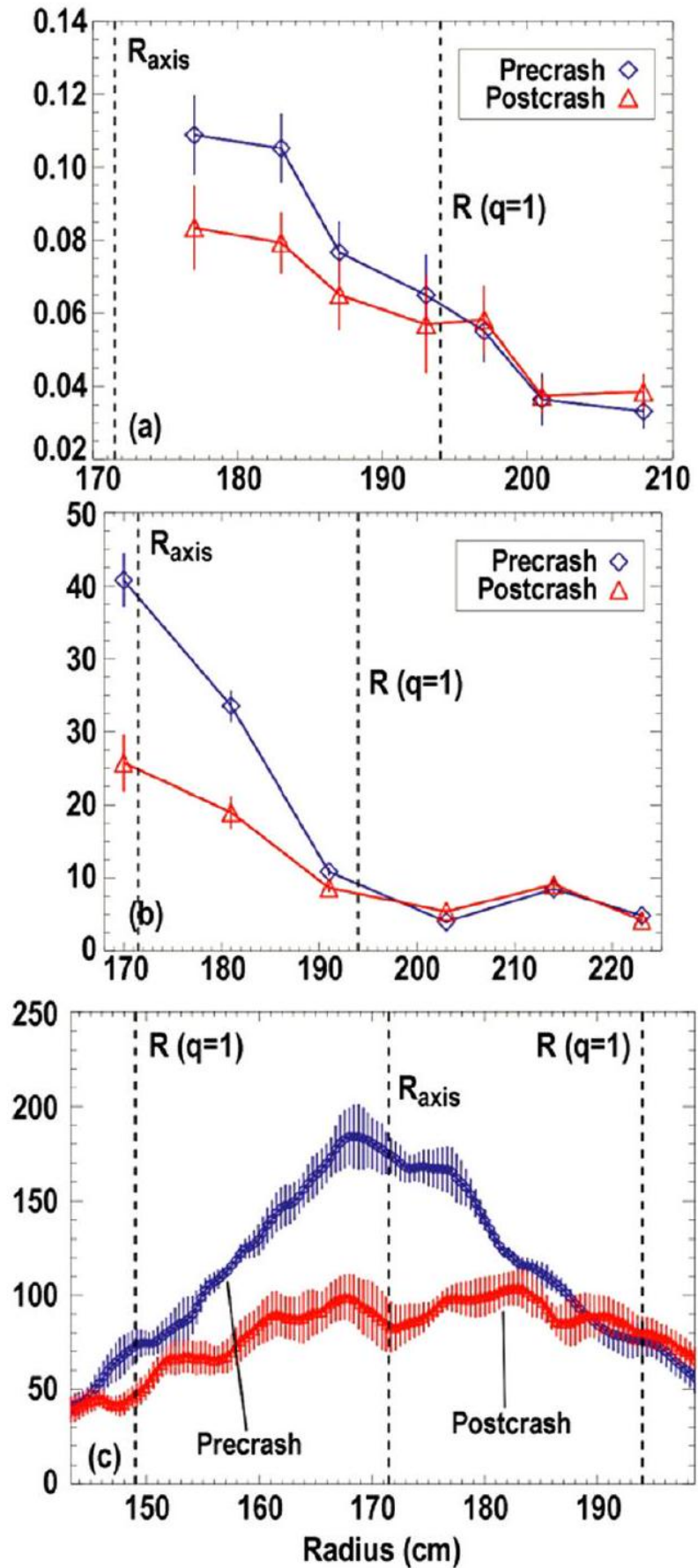


**Figure 36:** Radial profiles at the midplane proportional to the fast-ion density just before and just after an average sawtooth crash. The major radii of the magnetic axis and the  $q = 1$  surface are denoted. (a) Trapped fast ions (detected by the vertical FIDA system). (b) Co-circulating fast ions (detected by the near-tangential FIDAsystem). (c) Counter-circulating fast ions (detected by the FIDA imaging system). The 1D radial profiles from the imaging system are extracted from pixels that detect signal along the midplane.

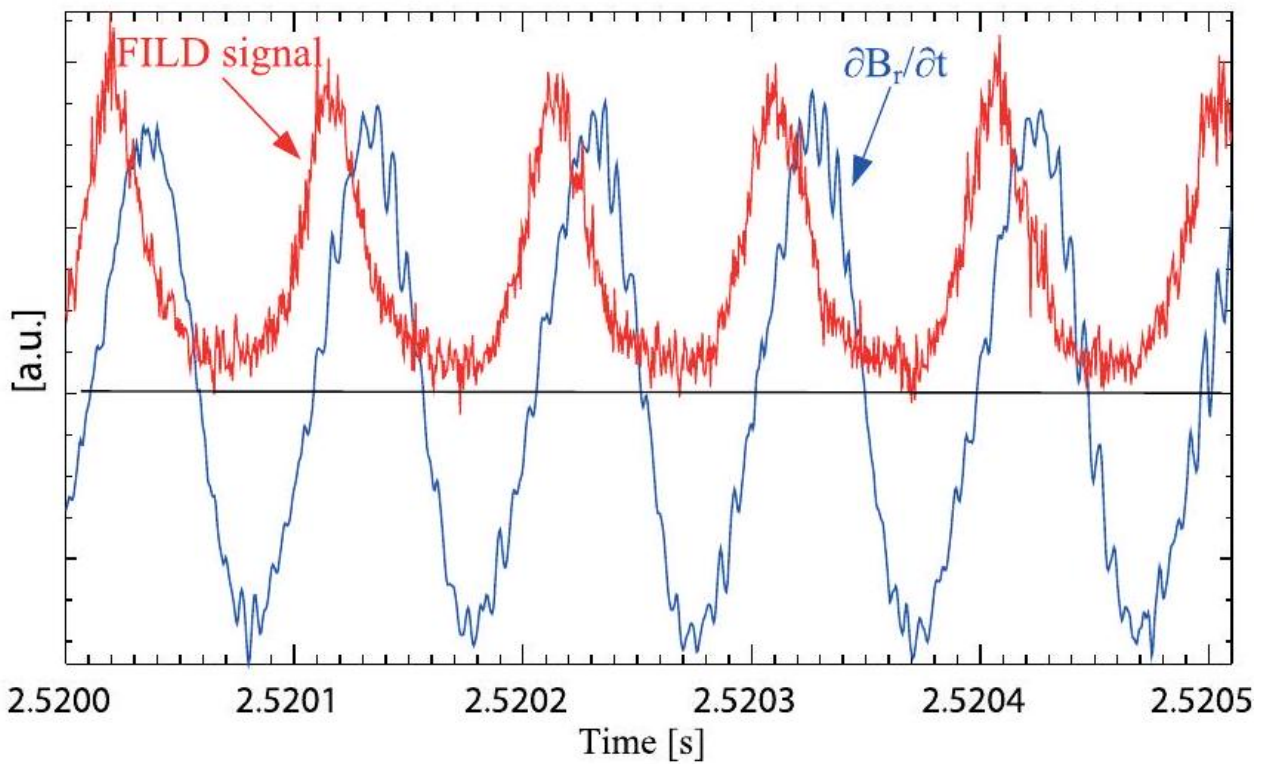


**Figure 37:** ASDEX Upgrade discharge #21081: Phase correlation between fast ion losses and the Mirnov signal  $\partial B_r / \partial t$  due to the magnetic island. Reprinted with permission from E. Poli et al., "Observation and modeling of fast trapped ion losses due to neoclassical tearing modes," *Phys. Plasmas* 15(3), 032501 (2008). Copyright 2008 American Institute of Physics.

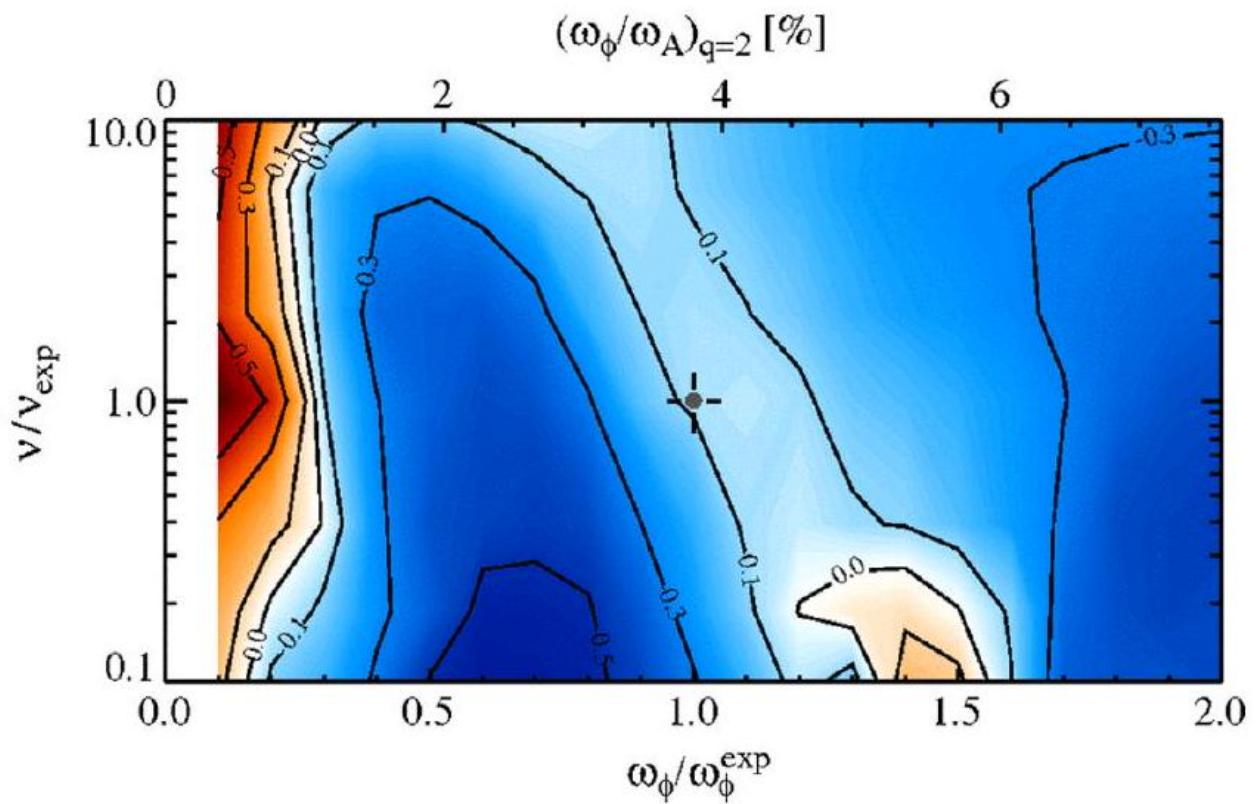


**Figure 38:** Contours of the RWM growth/damping rate (shown as  $\gamma\tau_w$ , where  $\tau_w$  is the wall time) for various collisionalities and rotation scaled to the experimental case in NSTX. Blue shows stable regions, red unstable. The growth rate is clearly non-monotonic with rotation. Reprinted with permission from J. W. Berkery et al., "Resistive wall mode instability at intermediate plasma rotation," Phys. Rev. Lett. 104(3), 035003 (2010). Copyright 2010 American Physical Society.

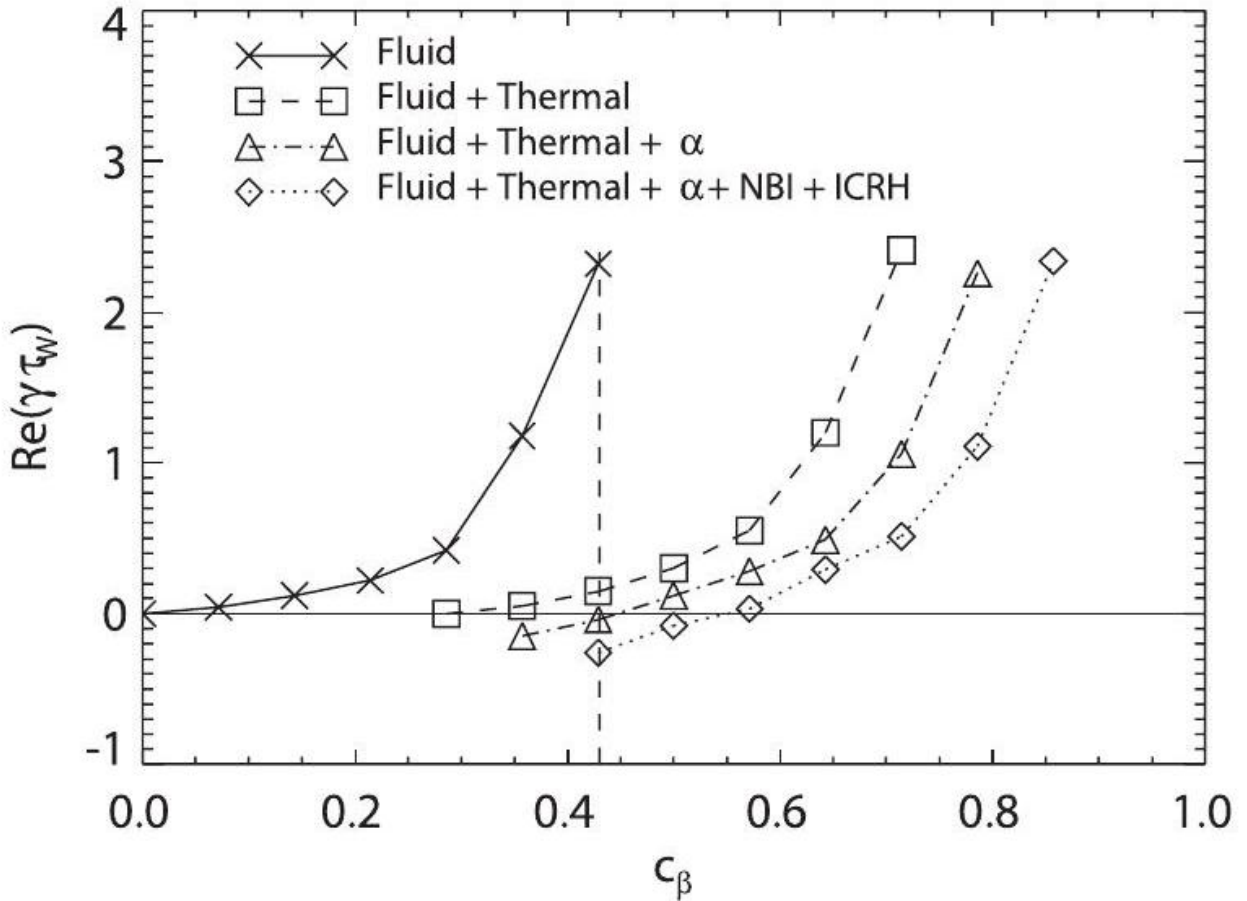


**Figure 39:** The growth or damping rate of the RWM in the ITER 9MA steady-state scenario found using the change in the mode potential energy associated with kinetic effects, as a function of  $C_\beta = (\beta - \beta_\infty) / (\beta_b - \beta_\infty)$  when only ideal fluid stability is considered or when additional damping from thermal and fast ion populations are considered for a rotation speed at the magnetic axis in ITER of  $v = 0.01v_A$ .<sup>129</sup> The marginal stability point is increased significantly by including all these damping effects, only made possible by including finite orbit width effects. The target value of  $C_\beta$  to achieve  $Q = 5$  in the ITER 9MA steady-state scenario is  $C_\beta = 0.43$  and corresponds to the vertical dashed line. Reprinted with permission from I. T. Chapman et al., "Kinetic damping of resistive wall modes in ITER," *Phys. Plasmas* 19(5), 052502 (2012). Copyright 2012 American Institute of Physics.

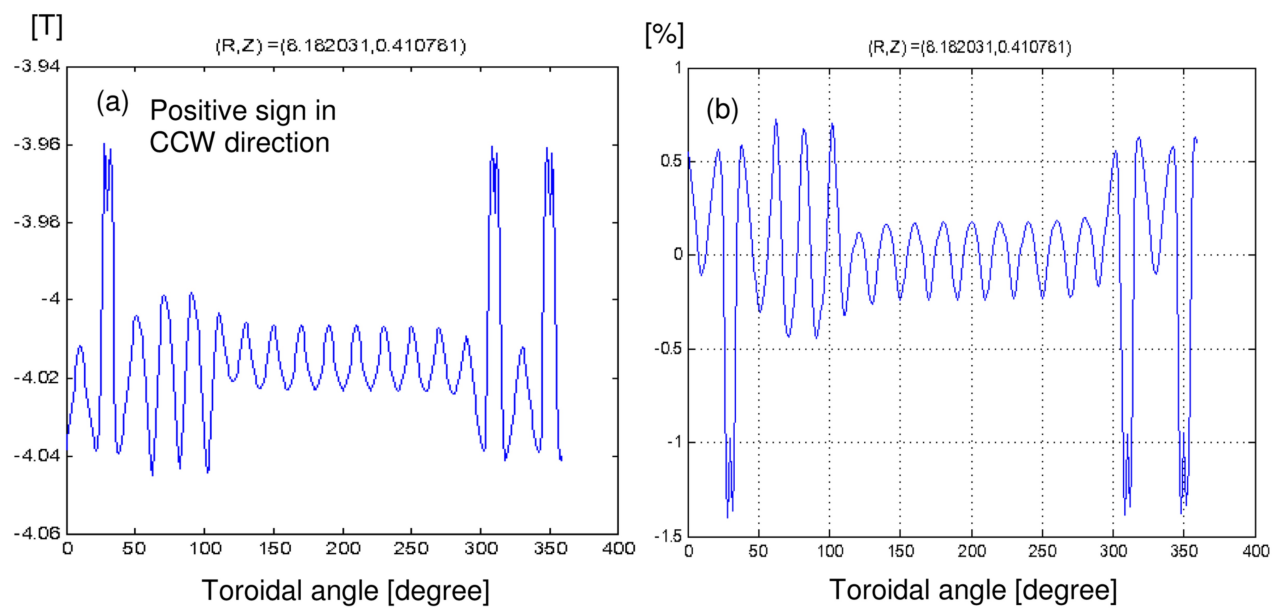


**Figure 40:** (a) Toroidal variation of the toroidal magnetic field,  $B_T$ . (b) Toroidal variation of the toroidal magnetic field ripple  $(B_T - \langle B_T \rangle) / \langle B_T \rangle$  at  $(R, Z) = (8.18 \text{ m}, 0.41 \text{ m})$  in ITER.

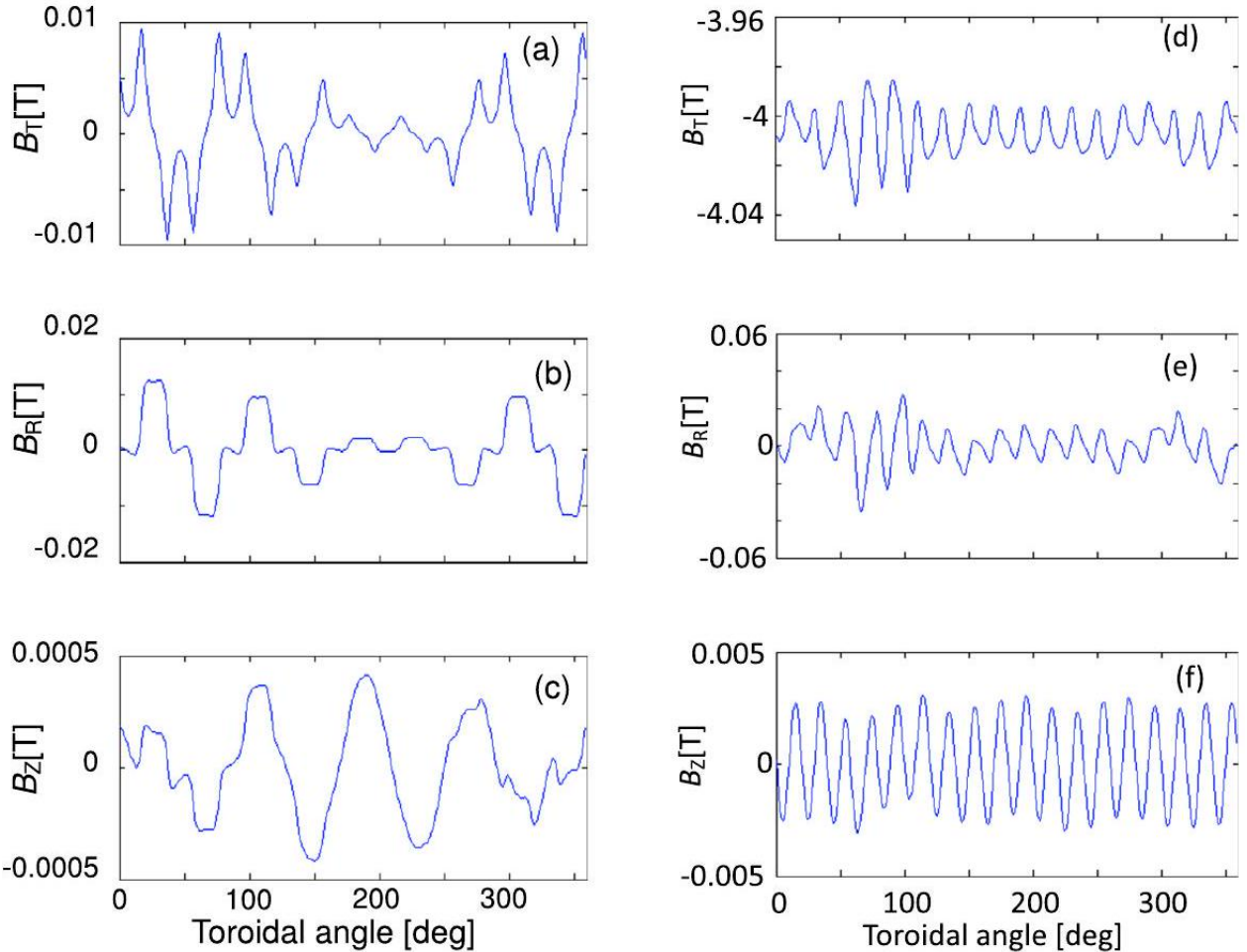


**Figure 41:** Magnetic field variation at the position of  $(R, Z) = (8.2 \text{ m}, 0.6 \text{ m})$ , i.e., near the separatrix outer midplane, for a current in the ELM control coils of 30kAt. This corresponds to the minimum coil current required to achieve the level of edge magnetic field perturbation to achieve ELM control on the basis of vacuum field estimates for a  $n = 4$  cosine waveform and the 15MA baseline scenario. (a)-(c) are for the field produced solely by the ELM control coils. (d)-(f) are for the field by TF

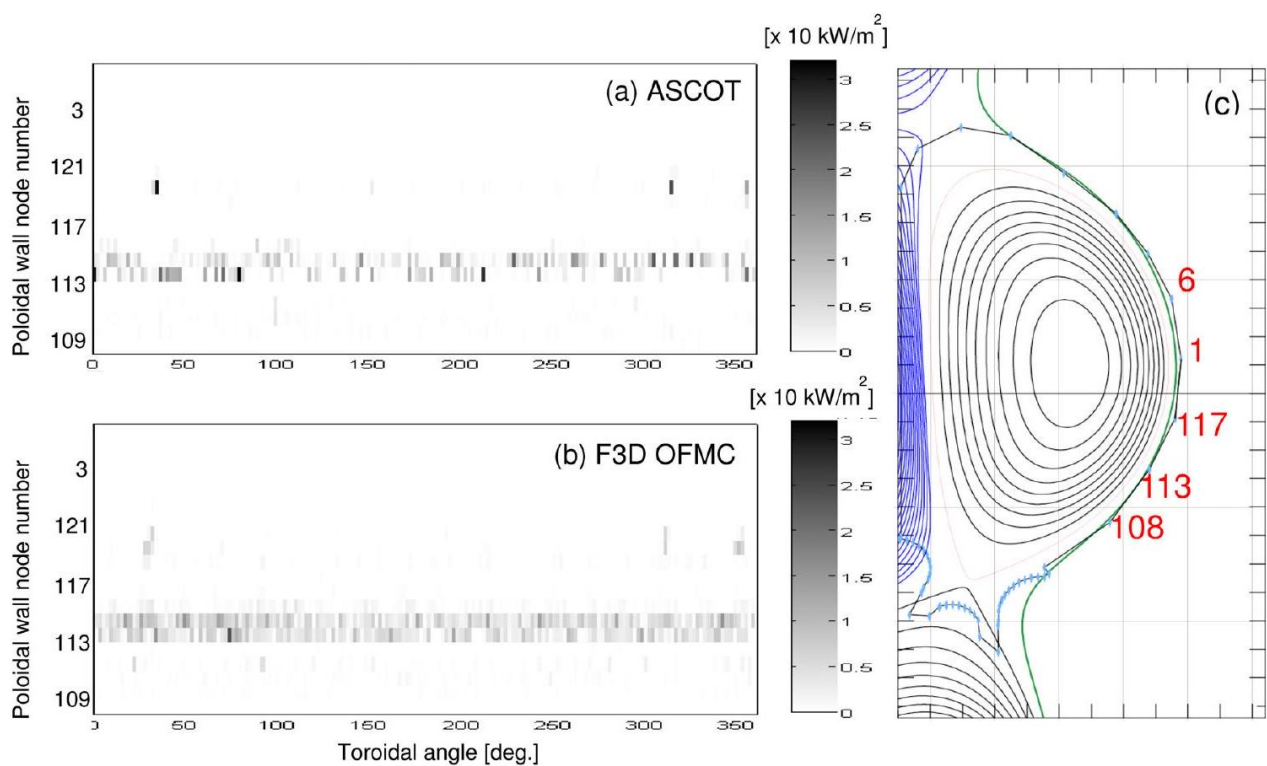


**Figure 42:** Heat load distribution for ASCOT (a) and F3D OFMC (b) for the 9 MA  $Q = 5$  ITER scenario. The horizontal axis is the toroidal angle. The vertical axis is the poloidal wall node number as illustrated in (c). Reprinted with permission from K. Shinohara et al., "Effects of complex symmetry-breakings on alpha particle power loads on first wall structures and equilibrium in ITER," Nucl. Fusion 51(6), 063 028 (2011). Copyright 1995 IAEA.

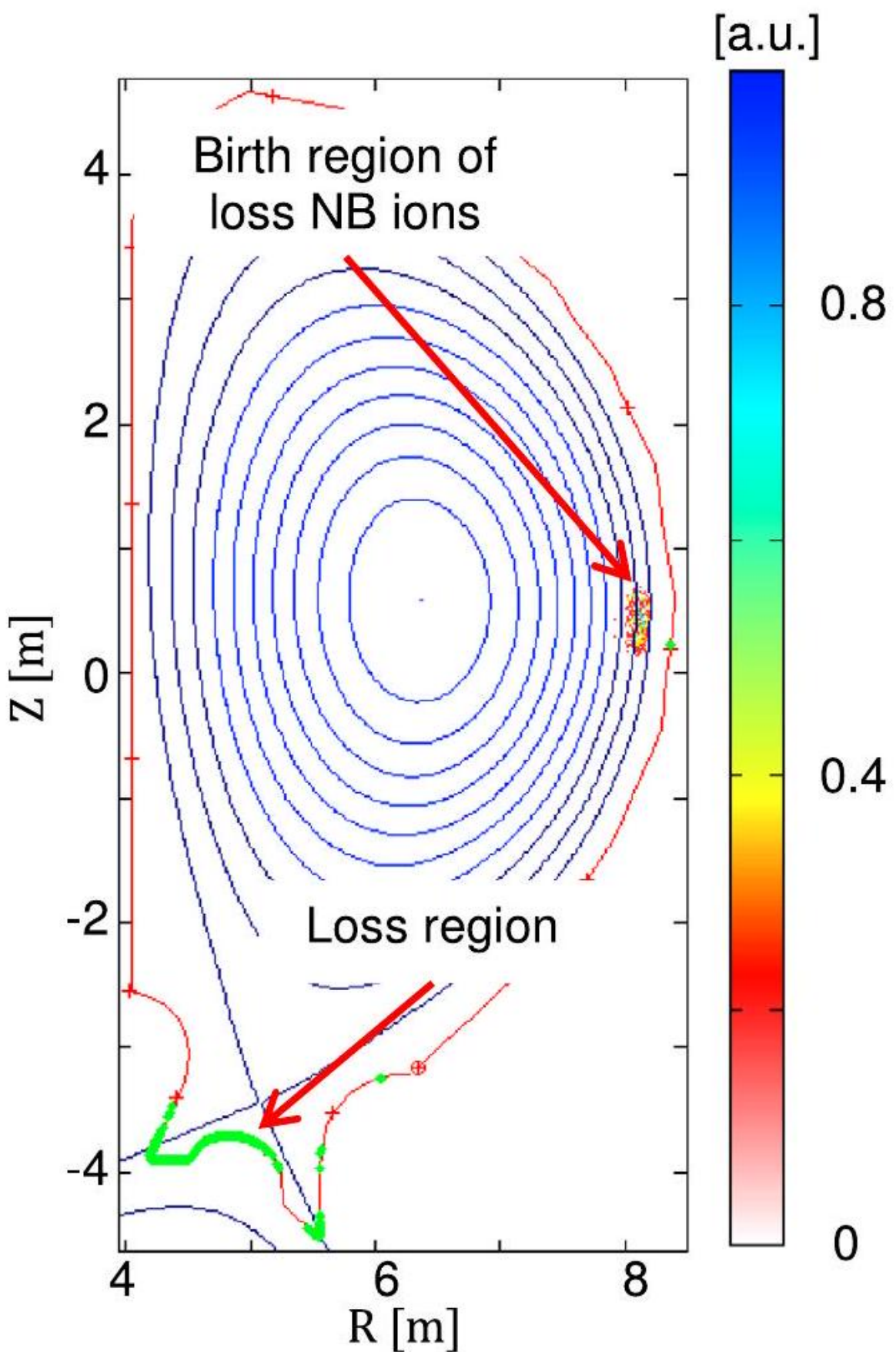


Figure 43: Origin of lost NB ions and points of impact of lost NB ions.